ORIGINAL PAPER

The Analysis of the Fracturing Mechanism and Brittleness Characteristics of Anisotropic Shale Based on Finite-Discrete Element Method

Hongtao Li[1] · David N. Chapman[1] · Asaad Faramarzi[1] · Nicole Metje[1]

Abstract

Shale anisotropy characteristics have great effects on the mechanical behaviour of the rock. Understanding shale anisotropic behaviour is one of the key interests to several geo-engineering fields, including tunnel, nuclear waste disposal and hydraulic fracturing. This research adopted the finite discrete element method (FDEM) to create anisotropic shale models in ABAQUS. The FDEM models were calibrated using the mechanical values obtained from published laboratory tests on Longmaxi shale. The results show that the anisotropic features of shale significantly affect the brittleness and fracturing mechanism at the micro-crack level. The total fracture number in shale under the Uniaxial Compressive Strength (UCS) test is not only related to the brittleness of shale. It is also strongly dependent on the structure of the shale, which is sensitive to shale anisotropy. Two new brittleness indices, BI_f and BI_{CD}, have been proposed in this paper. The expression for BI_f directly incorporates the number of fractures formed inside of the rock, which provides a more accurate frac-ability using this brittleness index. It can be used to calculate the frac-ability of rocks in projects where there are concerns about fractures after excavation. Meanwhile, BI_{CD} links brittleness to the CD/UCS ratio in shale for the first time. BI_{CD} is easy to obtain in comparison to other brittleness indices because it is based on the Uniaxial Compressive Strength test only. In addition, it has been shown there is a relationship between tensile strength and the crack damage strength in shale. Based on this, an empirical relationship has been proposed to predict the tensile strength based on the Uniaxial Compressive Strength test.

Highlights

- Through the use of FDEM simulations, the fracturing mechanics of shale, fracturing behaviour, and brittleness ofshale have been investigated from a micro-scopic viewpoint taking shale anisotropy into account.
- Two new brittleness indices are proposed. One relies on the number of fractures in the shale to reflect the shale'sfrac-ability, and the other uses strength parameters that can be easily obtained from UCS tests.
- This paper proposes an empirical relationship to predict the tensile strength of rocks based on UCS tests.

✉ Hongtao Li
hxl823@student.bham.ac.uk

1   School of Engineering, University of Birmingham, Birmingham B15 2TT, UK

1 Introduction

As a distinctively layered material, shale is widely introduced as anisotropic rock (Lisjak et al. 2014; Yang et al. 2020). During the past few decades, anisotropic mechanical properties of shale have been investigated at both the micro- and macro-scales (Ortega et al. 2007; Xian et al. 2019; Duan et al. 2015). Based on digital microscope images, Kasyap

and Senetakis (2022) have found that the shale microstructure with strong directions contributes to the anisotropic characteristics. As a result of comparing three different shales, Patel et al. (2022) also found that clay-rich shales have stronger anisotropic characteristics. This aligns with Wu et al. (2020) stating that clay minerals show stronger anisotropy than other minerals (i.e., quartz and feldspar) in shale. While the mineral composition is important, it is the existence of bedding planes that work as weakening planes in the shale matrix significantly which affects the shale's strength and fracturing mechanism in macro scale (Yang et al. 2020; Popp et al. 2008). The orientation of these bedding planes within shale significantly contributes to the anisotropic properties of the shale. In the past decades, many researchers have conducted various laboratory tests to explore the anisotropic properties of shale and studied the macro mechanical responses of shale under Uniaxial Compressive Strength (UCS) tests with samples obtained from various places worldwide (Yang et al. 2020; Heng et al. 2020). Based on UCS test results on different shales from around the world against the bedding planes inclinations, shales can be generally classified into three types, i.e., "U-shaped", "shoulder shaped" and "wavy shaped" (Fjær and Nes 2014; Ali et al. 2014). In 1960, Jaeger proposed a failure criterion to describe shale strength anisotropy by introducing a single weakening plane in the shale matrix (Jaeger 1960). Subsequently, several researchers have tried to introduce more failure models for the anisotropy of shale based on laboratory tests on shale strengths and failure behaviour (Hoek and Brown 1980; Ramamurthy et al. 1988). The influence of the anisotropic behaviours of shale on the tensile strength is also studied by a few researchers. Their studies show that the tensile strength of shale decreases with increasing dip angles of the bedding planes (Cao et al. 2020; Wang et al. 2018a, b). Meanwhile, Geng et al. (2016) found that all shale samples with different bedding plane inclinations (15°, 30°, 45°, 60°, 75°, 90°) increase in peak strength with increasing confining pressure, except for the 0° sample. Several studies have also observed that the confining pressure can affect the shale's anisotropy (Bonnelye et al. 2017; Jiang et al. 2019; Li et al. 2020). On the other hand, a limited number of studies has also investigated the relationship between shale micromechanical properties and anisotropy (Abousleiman et al. 2007). Keller et al. (2017) have found that the micro-scale anisotropy of the clay matrix is more severe than the macro-scale mechanical values of shale based on nanoindentation testing, which also agrees with the findings of Wu et al. (2021).

As mentioned above, most of the studies investigating the anisotropic properties of shale have focused on macro mechanical strengths. Based on the stress–strain curve of the shale sample under compression, it appears that the mechanical response of shale is affected by fracture forming and propagating (Lisjak and Grasselli 2014; Bieniawski 1967). Additionally, the sensitivity of the crack damage stress (CD) threshold to shale anisotropy indicates that shale anisotropy affects its macro mechanical strength from a micro-crack level (Li et al. 2020). However, the understanding of shale macro mechanical strength from micro-crack level (e.g., fracturing mechanism and fracturing conditions) still remains as an open book. Meanwhile, brittleness is an important parameter in assessing the mechanical properties of rocks (Niandou et al. 1997; Suo et al. 2020; Chandler et al. 2016). However, currently, there is not yet a universal definition of rock brittleness. A large body of research has studied the shale brittleness influencing factors, such as material internal geological factors, environmental factors and geo-stress differences (Wang et al. 2016a, b; Jarvie et al. 2007; Ai et al. 2016; Hucka and Das 1974). On that basis, many researchers have proposed different rock brittleness indices based on, for example, rock strength, stress–strain curve and components analysis (Jarvie et al. 2007; Bishop 1971; Munoz et al. 2016). Based on its mechanical properties, shale can be classified as either brittle or ductile (Nygård et al. 2006). Comparing to ductile shale, brittle shales more easily fracture. Frac-ability of shale has been widely described as the rock brittleness in hydraulic fracturing (Rybacki et al. 2016; Bai 2016). Therefore, the brittleness of shale not only relies on the former mentioned factors but also on the fracturing mechanism of shale.

In recent decades, numerical modelling has been increasingly adopted to study some complex geotechnical problems. Particularly with the pervasive development of computer hardware and software, numerical modelling has become a widely used method to simulate different geotechnical situations. Numerical approaches used in computational geomechanics can be classified as (i) continuum methods; (ii) discrete element methods (DEM); and (iii) hybrid finite-discrete element methods (FDEM).

Over the past few decades, the Finite element method (FEM), as one of the most popular numerical methods, has often been used to study layered rocks (Doležalová 2001; Hao et al. 2016) using either explicit or implicit approaches to account for the discontinuities inside of rocks. The implicit approach, also called the smeared approach, considers the rock with joints as a fictitious homogenised material that exhibits similar mechanical properties compared to the original rocks. The most widely used smeared approach considers the rock mass as continuous with reduced deformation modulus and strength parameters (Huang et al. 2009; Wang et al. 2018a, b). Models for transversely isotropic elastic rocks and columnar joint rocks have also been introduced (Amadei 1996). However, the localised large deformation around discontinuities (e.g., slip, rotations, and separation) cannot be captured by this homogenisation approach (Hammah et al. 2008). The explicit approach, in contrast,

considers the discontinuities separately from the continuum formations. This explicit approach to modelling the discontinuities inside rocks can also be classified into two approaches. The first approach to modelling the properties of discontinuities using specific elastic elements was first introduced by Goodman (1968). The stress and strain around this fictional elastic element, also called a 'joint element', is in a linear elastic relationship. With the development of this theory, more joint elements with different mechanical properties, such as plastic behaviour and elastoplastic behaviour, have been proposed (Zienkiewicz et al. 1970; Ghaboussi et al. 1973).

An alternative numerical approach, DEM was first introduced by Cundall (1971) to solve rock mechanical problems. With this approach, the macro-scale failure of the rock can be investigated from a microscopic particle scale (Duan et al. 2015; Ivars et al. 2011). The bonded-particle model (BPM) allows the initiation and propagation of the crack forming from a micro-scale to a macro-scale to be explicitly traced inside a rock without applying parameter assumptions and complex constitutive laws (Potyondy and Cundall 2004). Within the BPM, the particles are bonded together, and once the applied strength exceeds the corresponding bond strength, the discrete particles can move relative to each other. Previous research has shown that the crack formation and propagation in shale rock is mainly due to the relative movement of the clay particles (Fabre and Pellet 2006). Under a scanning electron microscope (SEM), the face-to-face clay particle adjustment along these micro-cracking planes has been observed (Raynaud et al. 2008). In this case, DEM can capture this feature of the rock perfectly as it treats the material directly as an assembly of bonded blocks or particles. However, most geotechnical DEM modelling is conducted at a laboratory-scale due to the limitations of computational capacity (Ivars et al. 2011; Yimsiri and Soga 2010). The size of the shale rock particles can be discretised to micrometre clay-sized particles. However, there would be millions of particles and at a field-scale model with the size of tens of metres, which would result in an unacceptable computational time.

The hybrid finite-discrete element method (FDEM) was first introduced by Munjiza (2004). The FDEM has adopted continuum mechanics principles to govern the small strain changes in the elastic and cohesive elements, while DEM algorithms are used to trace the interaction of the elastic elements once the cohesion crack elements are broken. The last decade has seen the increasing popularity of using the FDEM approach to simulate the fracturing in the materials (Chen et al. 2020; Fukuda et al. 2021; Wei et al. 2019; Ma et al. 2019). This method has also been used to simulate different geo-mechanical problems, such as tunnelling (Lisjak et al. 2014, 2020), rockslides (Zhou et al. 2016) and hydraulic fracturing (Yan et al. 2016).

This paper aims to investigate the shale fracturing mechanics, fracturing behaviour and brittleness from a microscopic viewpoint taking the shale anisotropy into account through FDEM simulation. Two new brittleness indices are proposed based on the results and analysis. One relies on the number of fractures in the shale to reflect shale's frac-ability, and the other uses strength parameters that can be obtained easily from UCS tests. This is the first study to link brittleness to the CD/UCS ratio in shale. In addition, this paper proposes an empirical relationship to predict the tensile strength of rocks based on UCS tests.

Following is the organisation of the paper. Shale laboratory scale FDEM models are developed to model shale anisotropic deformation and strength characteristics through ABAQUS. Laboratory scale FDEM models are then validated by quantitatively reproducing laboratory test results (i.e., uniaxial compression strength (UCS) and Brazilian disc (BD) tests) of Longamxi shale. Finally, the effects of shale anisotropy on the failure mechanism and brittleness from the micro-crack level are analysed through the verified FDEM small-scale laboratory shale model with different bedding plane inclinations.

2 Modelling Shale Anisotropy in FDEM

In FDEM, the modelling domain is discretised into three-node triangular elements with four-node rectangular cohesive elements between the triangular elements, as shown in Fig. 1. The combined FDEM has adopted continuum mechanics principles to govern small strain changes in the
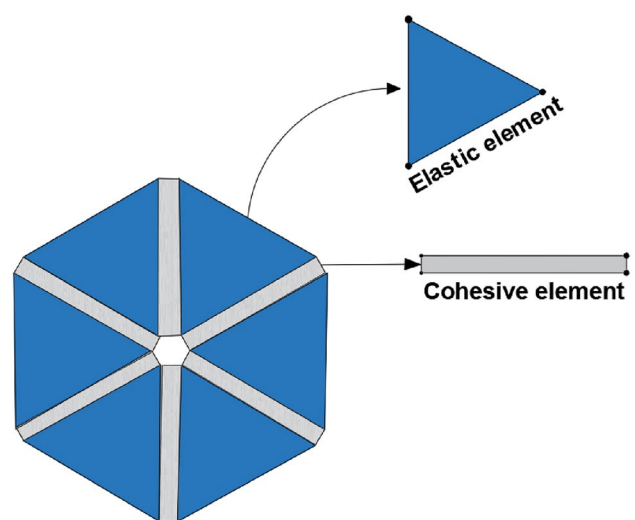

Fig. 1 Diagram of a domain meshed by FDEM

elastic and cohesive elements, while DEM algorithms are used to trace the interaction between the elastic bulk elements after the cohesive elements have 'failed' and cracks formed. The transformation of the domain from continuous to discontinuous is, therefore, realised by breaking and deleting the 'failed' cohesive elements, known as the cohesive zone model (CZM), to simulate fracture initiation and propagation (Chandra et al. 2002).

The anisotropic characteristics of shale are mainly controlled by the bedding planes distributed within it, which leads to the deformation of the shale showing strong isotropic properties within the bedding planes (Hakala et al. 2007; Amadei 1996). Shale, in this case, has been classified as a transverse isotropic material. These bedding planes act as discontinues or joints in the shale matrix due to their lower stiffness and strength when compared to the matrix. In FDEM, the cohesive elements act as interfaces between adjacent elastic elements, which is similar to the composition of the shale. The shale matrix is discretised by bedding planes and can therefore be ideally modelled by this new modelling method within the framework of the FDEM. A smeared approach introduced by Lisjak et al. (2014) has been commonly accepted to model shale in FDEM. The smeared approach assumes that the macroscopical strength anisotropy of rock is the result of cohesive element anisotropy. Similarly, Li and Zhang (2019) have proposed a shale model that assigns different cohesive laws to the cohesive elements in the shale matrix and bedding planes. Hence, this study developed an FDEM shale model using the smear approach in ABAQUS to investigate the effects of anisotropy on the fracturing mechanism, fracture behaviours, and brittleness in shale. Based on a Python code, the FDEM shale model was created in ABAQUS to model the structural characteristics by following the steps below:
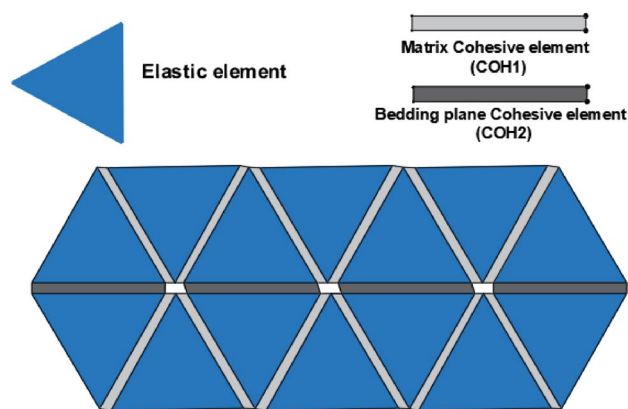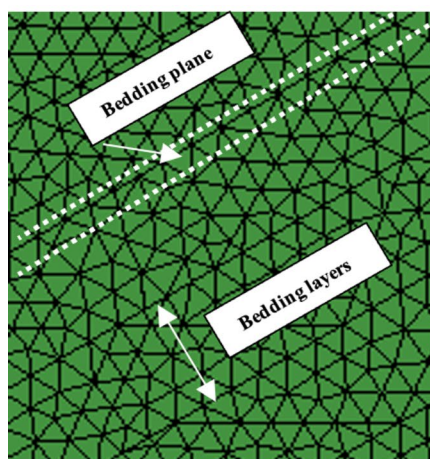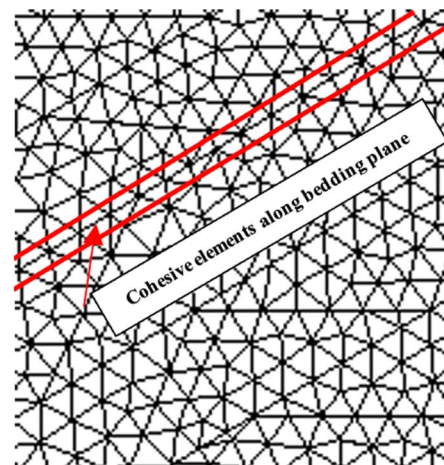

Fig. 3 The distribution of the two different cohesive elements

(1) Meshing the intra-layer shale matrix using a random triangulation method, ensuring the elastic elements are aligned along the direction of the bedding planes, as shown in Fig. 2a. The bedding planes in the shale FDEM model are then realised by assigning different parameters into the cohesive elements of the matrix and bedding planes based on the smear approach (Lisjak et al. 2014).

(2) As shown in Fig. 2b, cohesive elements are inserted into adjacent elastic elements using a Python-based code.

(3) Assigning different cohesive strength parameters to different cohesive elements. The cohesive elements inside the shale model can be divided into two different types, matrix cohesive elements and bedding plane cohesive elements. As shown in Fig. 3, the matrix cohesive elements (COH1) are distributed inside the shale matrix with strong cohesive strength parameters, while the bedding plane cohesive elements (COH2) are assigned

Fig. 2 Modelling shale anisotropy in FDEM. **a** Mesh topology. **b** Cohesive element alignment

a) Mesh topology

b) Cohesive element alignment

| Approaches	Formulae	Notes
Mineral composition	$BI_1 = W_Q/W_{Q+C+Cl}$	W_Q = quartz, C = carbonate, Cl = clay
Strength parameters	$BI_2 = \sigma_u/\sigma_t$	σ_u = uniaxial compressive strength, σ_t = Brazilian tensile strength
Stress–strain curves	$BI_3 = (\sigma_f - \sigma_r)/\sigma_f$	σ_f = stress at failure, σ_r = residual strength, ε_e = elastic strain,
	$BI_4 = \varepsilon_e/\varepsilon_t$	ε_t = total strain at failure
Energy balance analysis	$BI_5 = U_{et} / (U_{et} + U_p)$	U_{et} = total elastic energy, U_p = plastic energy, U_r = rupture
	$BI_6 = U_r/U_{ec}$	energy, U_{ec} = consumed elastic energy
	$BI_7 = U_{et} / (U_r + U_p)$	
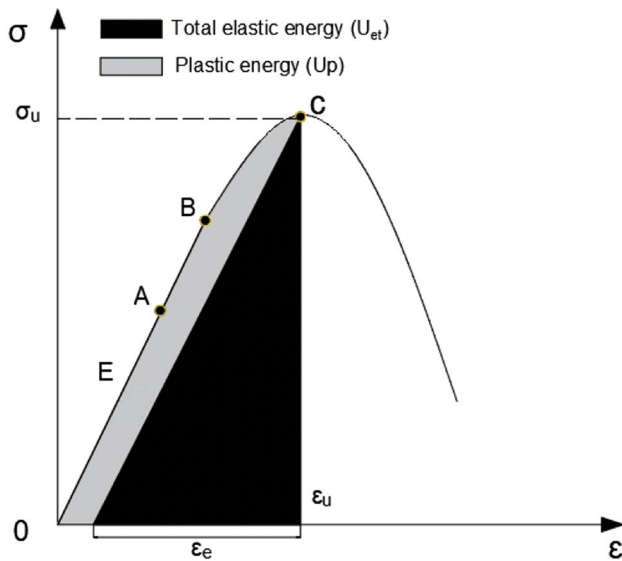
Fig. 4 Energy evolution of rock during compression (Point A: crack initiation stress (*CI*), point B: crack damage stress (*CD*), point C: Uniaxial compressive strength)

along the bedding plane with weak cohesive strength parameters.

3 Evaluation of the Approaches to Determine Shale Brittleness

To quantify the brittleness of the rock mass, several brittleness indices (BI) have been introduced by different researchers. These BIs can be classified into four main approaches, in terms of mineral composition, strength parameters, stress–strain characteristics and energy balance analyses, which are the main influencing factors of rock brittleness, as shown in Table 1.

It has been found that the results based only on the strength or strain BI could be contradictory in some cases,

as these BIs only consider some characteristics of the shale (He et al. 2021). For example, different rock types with the same strength have different displacements, which would lead to different conclusions about the rock brittleness based on different BIs (Hucka and Das 1974).

A rock specimen under a traditional UCS test can be treated as a process of energy absorption and release (Kivi et al. 2018). The evolution of the energy within the stress–strain curve can be divided into two phases: the pre-peak and post-peak stages. This paper discusses the fractures forming inside shale samples before macro-failure, which is essential to understanding the fracture formation and propagation at the pre-peak phase. As shown in Fig. 4, the pre-peak phase of the energy evolution of the rock can be illustrated through the stress–strain curve (and more specifically the area under the stress–strain curve). Before reaching the uniaxial strength of the shale (point C), the energy evolution phase can be divided into two parts. In the elastic deformation part, the rock materials steadily absorb external energy, which is then stored as elastic energy in the rock. Once the stress in the rock reaches point A (Fig. 4), where cracks are starting to form in the rock, a portion of the absorbed energy dissipates due to internal damage. This internal damage includes fracture formation, propagation, and the internal friction between the particles, reflected as unrecoverable plastic deformation in the stress–strain curve. The black area in Fig. 4 is the elastic energy stored in the rock before macro failure, which is the energy source for the post-peak rock failure. Meanwhile, the grey area reveals the plastic energy, which has been consumed by internal damage.

Based on Fig. 4, the elastic energy U_{et} is given by Eq. (1).

$$U_{et} = \frac{1}{2E}\sigma_u^2 \tag{1}$$

where E is the Young's modulus of the rock, and σ_u is the uniaxial compressive strength.

Also based on Fig. 4, the energy U_t is given by Eq. (2), where σ and ε represents stress and strain, respectively.

$$U_t = \int_0^{\varepsilon_u} \sigma d\varepsilon \tag{2}$$

Hence, the equation of the brittleness index BI_5 from Table 1 can also be written as:

$$BI_5 = \frac{\sigma_u 2}{2E\int_0^{\varepsilon_u} \sigma d\varepsilon} \tag{3}$$

4 Simulating Laboratory Tests on Longmaxi Shale

4.1 Model Description

The capacity of FDEM to model the mechanical and failure behaviour of shale has been verified through UCS and BD tests on Longmaxi shale. A two-dimensional 100 mm × 50 mm rectangular numerical model and a 50 mm diameter circular numerical model were created for the UCS and BD tests, respectively. The cross-section of each model was assumed to lie perpendicular to the strike of the bedding planes. Hence, the anisotropy of the shale in different directions was realised by changing the inclination of the bedding planes in the models as shown in Fig. 5. The specimens were meshed in the mesh topology as discussed previously (Sect. 2) and the intra-layers were meshed into uniform and unstructured triangular grids, while the cohesive elements were preferentially aligned along the direction of the bedding planes.

The model mesh and layer thickness sensitivity have been studied. This research investigated the element size sensitivity of the FDEM shale model by simulating the response
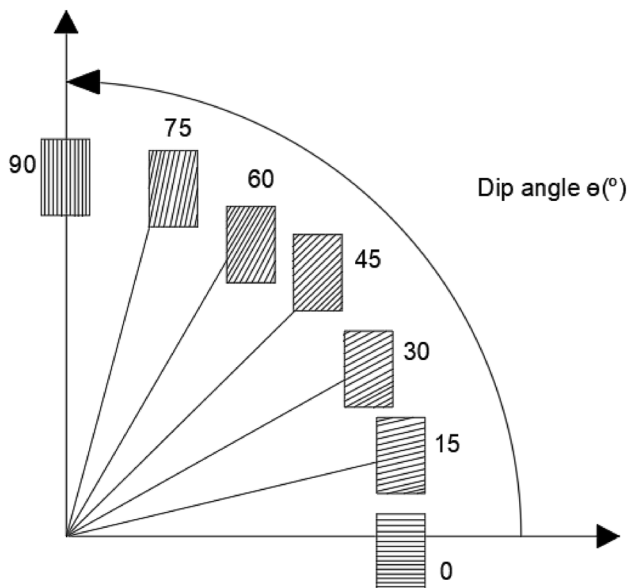

Fig. 5 Diagram of different bedding plane inclinations in the shale FDEM models

of the UCS test model at 0° inclination with element sizes ranging from 0.5 to 3 mm. The shale uniaxial compressive strength converges to the laboratory measurements with decreasing element size, as shown in Fig. 6a. With reducing element size, the computational cost increases. Figure 6a clearly illustrates that shale models with 0.8 and 1 mm average element sizes yield a UCS that is close to the laboratory values even though the convergence to a steady result occurs at smaller element sizes. However, the difference between this steady state result for UCS and the one obtained with an element size of 0.3 mm is minimal, while the additional computational effort would be significant. Thus, it was decided to adopt an element size of 0.8 mm as a compromise between having reached steady state conditions and computational effort. Meanwhile, the layer thickness effects on the model have also been studied by simulating the response of the UCS test model at 0°, 45° and 90° bedding plane inclinations with the layer thickness ranging from 2.5 to 17.5 mm. According to Fig. 6b, the shale model with a bedding plane inclination of 0° showed that the layer thickness had no effect on the UCS. Conversely, the modelled UCS values of the shale models with bedding planes inclined at 45° and 90° increased with increasing layer thickness. The peak strength in the shale model with 45° and 90° inclinations converges with layer thicknesses smaller than 5 mm. Hence, this study has adopted a layer thickness of 2.5 mm.

The loading platens, placed on the top and bottom of the specimen, were moved in opposite directions as shown in Fig. 7. In the numerical simulation, a lower loading rate leads to a longer loading time, resulting in dramatically growing computational time. The loading rate of the two platens is 50 mm/s, which is much greater than the 1.8 mm/min used in the experiments. However, the simulated strengths were found to approach constant values close to the experimental values when the loading rates were lower than 150 mm/s based on a loading rate sensitivity study. Meanwhile, Fig. 6c shows the Poisson's ratio of Longmaxi shale slightly increases as the loading rate increases. From 10 to 500 mm/s, the Poisson's ratio of Longmaxi only increased by 3.9%. Therefore, the influence of the loading rate on the Poisson's ratio of Longmaxi shale is limited.

The present study has adopted a two-dimensional simulation due to computational efficiency limitations. A two-dimensional model has certain limitations compared to a three-dimensional model, including the initiation and propagation of fractures in the rock occurring in three dimensions. There is no consideration of out-of-plane deformation or interactions between cracks that occur in different planes in two-dimensional models. To address this, a three-dimensional analysis should be considered in future works. Meanwhile, two-dimensional models provide a simplified representation of the crack behaviour in rocks, which still provides valuable information.
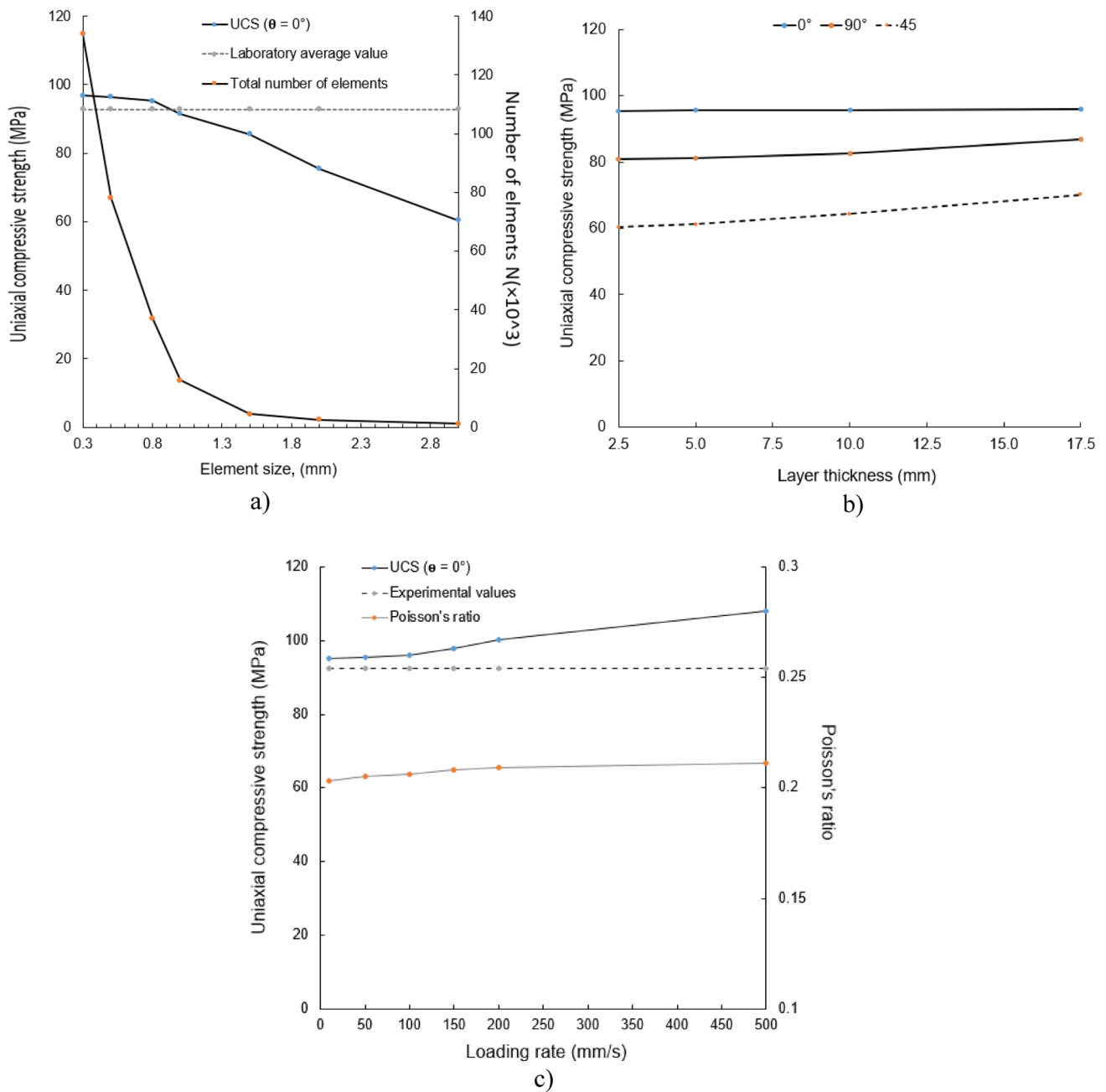
Fig. 6 The sensitivity study of element size and layer thickness. **a** Element size. **b** Layer thickness. **c** Loading rate

4.2 Model Calibration and Input Parameters

The FDEM numerical models of shale were calibrated against the UCS and BD experimental test results to characterise the short-term emergent mechanical response of Long-maxi shale. In this study, shale long-term creep behaviour was not considered. In future studies, exploring the long-term fracturing mechanisms of shale rock may help understand its creep behaviour. The critical parameters used as calibration targets were the uniaxial compressive strength and tensile strength. As both these mechanical properties show a strong anisotropic behaviour, the numerical models with bedding plane inclinations of 0° and 90° were considered.

For the FDEM model, both macro-scopic and micro-scopic parameters are needed (Munjiza 2004; Lisjak et al. 2014). Elastic elements require macro-scopic parameters (such as density, Young's modulus, Poisson's ratio, and shear modulus), while cohesive elements require micromechanical
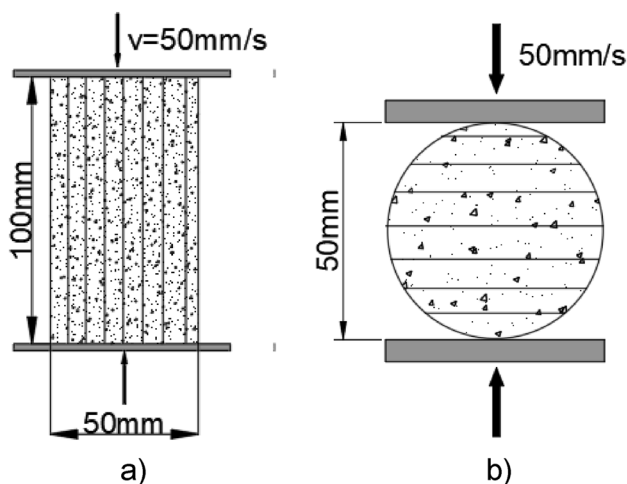
Fig. 7 The FDEM models created in ABAQUS. **a** UCS test FDEM model. **b** BD test FDEM model

parameters (such as tensile strength, cohesion, fracture energies, and stiffness). The elastic behaviour of transversely isotropic shale is characterised by five independent elastic constants: E_1, v_1, E_3, v_3, G_3 (Jaeger 1960; Lisjak et al. 2014). E_1 and v_1 are Young's Modulus and Poisson's ratio in the plane of the transverse isotropy, respectively. E_3, v_3 and G_3 are Young's Modulus, Poisson's ratio and shear modulus in the direction of the axis of rotational symmetry. Based on the sensitivity study of the cohesive element parameters by Deng et al. (2021), the tensile strengths and fracture energies are the main dominant parameters impacting the mechanical strength and also failure mode in the FDEM model. Accordingly, Deng et al. (2021) recommended that the values of the cohesion and friction angle of the cohesive element (i.e., macro-parameters) can be directly determined from laboratory tests. The material properties for the elastic elements (i.e., Young's modulus, Poisson's ratio and shear modulus), and the cohesive elements (friction angle and cohesion parameters gained from triaxial tests using Mohr–Coulomb criterion) were directly taken from the laboratory tests (Wang et al. 2018a, b, 2020; Ma et al. 2018). The cohesive elements tensile strength and fracture energy in Mode I and Mode II were modified to improve the numerical results for the UCS and BD tests. Meanwhile, based on Deng et al. (2021), the friction angle has no effect on the fracture energies. Therefore, the values for the friction angle of all elements are the same. The stiffness of the cohesive elements, as one of the model's critical parameters, can significantly affect the elastic response of the FDEM model. According to the study conducted by Yuan and Li (2014), a rock model is not sensitive to cohesive stiffness once the stiffness of the

Table 2 Input parameters for the Longmaxi shale FDEM model (Wang et al. 2018a, b; 2020; Ma et al. 2018)

Parameter	Value
Elastic elements	
Density, ρ (kg/m^3)	2586
Young's modulus parallel to bedding, E_{par} (GPa)	21.5
Young's modulus perpendicular to bedding, E_{per} (GPa)	14.6
Poisson's ratio parallel to bedding, ν_{par}	0.233
Poisson's ratio perpendicular to bedding, ν_{per}	0.22
Shear modulus, G (GPa)	9.08
Cohesive elements	
Tensile strength parallel to bedding, f_{tpar} (MPa)	1
Tensile strength perpendicular to bedding, f_{tper} (MPa)	2
Cohesion parallel to bedding, c_{par} (MPa)	8.9
Cohesion perpendicular to bedding, c_{per} (MPa)	16.2
Mode I fracture energy parallel to bedding, G_{Ifpar} (J/m^2)	30
Mode I fracture energy perpendicular to bedding, G_{Ifper} (J/m^2)	45
Mode II fracture energy parallel to bedding, G_{IIfpar} (J/m^2)	130
Mode II fracture energy perpendicular to bedding, G_{IIfper} (J/m^2)	350
Friction angle of intact material, φi (deg)	36.27
Normal stiffness, k_n (GPa/m)	250
Shear stiffness, k_s (GPa/m)	25
Element/Loading platen friction coefficient, C	0.1

cohesive element has exceeded the Young's modulus of the rock matrix. Based on the recommendation from Mahabadi et al. (2012) and Lisjak et al. (2014), the values of the cohesive normal and shear stiffness were set to ten times, and one times the Young's modulus of the rock matrix, respectively. The parameters adopted in the model are listed in Table 2.

Table 3 compares the mechanical properties of the numerical models with the values gained from experimental tests on Longmaxi shale. The relative errors for all values are within 5%.

4.3 Simulated Stress–Strain Response in Uniaxial Compression Strength Tests

The comparison of the laboratory tests and FDEM simulation for the stress–strain curves in the UCS tests on Longmaxi shale with bedding plane inclinations of 0° and 90° are shown in Fig. 8. In both shale models, the peak strength and slope of the stress–strain curves are close to those observed in the laboratory tests with minor differences (Wang et al. 2020). The stress–strain behaviour of the Longmaxi shale FDEM models can be divided into three phases that are typically observed in several brittle

Table 3 Comparison of the mechanical properties of the Longmaxi shale between the numerical model and experiment results (Wang et al. 2018a, b; 2020; Ma et al. 2018)

| Mechanical properties	Experimental value	Numerical value
Elastic modulus parallel to bedding, E_{Par} (GPa)	21.5 ± 0.2	22.200
Elastic modulus perpendicular to bedding, E_{per} (GPa)	14.8 ± 0.25	14.300
Poisson's ratio parallel to bedding, ν_{par}	0.233	0.252
Poisson's ratio perpendicular to bedding, ν_{per}	0.220	0.205
Uniaxial compressive strength parallel to bedding, σ_{uPar} (MPa)	76.800 ± 4	80.930
Uniaxial compressive strength perpendicular to bedding, σ_{uPar} (MPa)	92.170 ± 0.6	95.590
Indirect tensile strength parallel to bedding, σ_{tpar} (MPa)	3.500 ± 0.5	3.170
Indirect tensile strength perpendicular to bedding, σ_{tper} (MPa)	6.600 ± 0.7	6.570
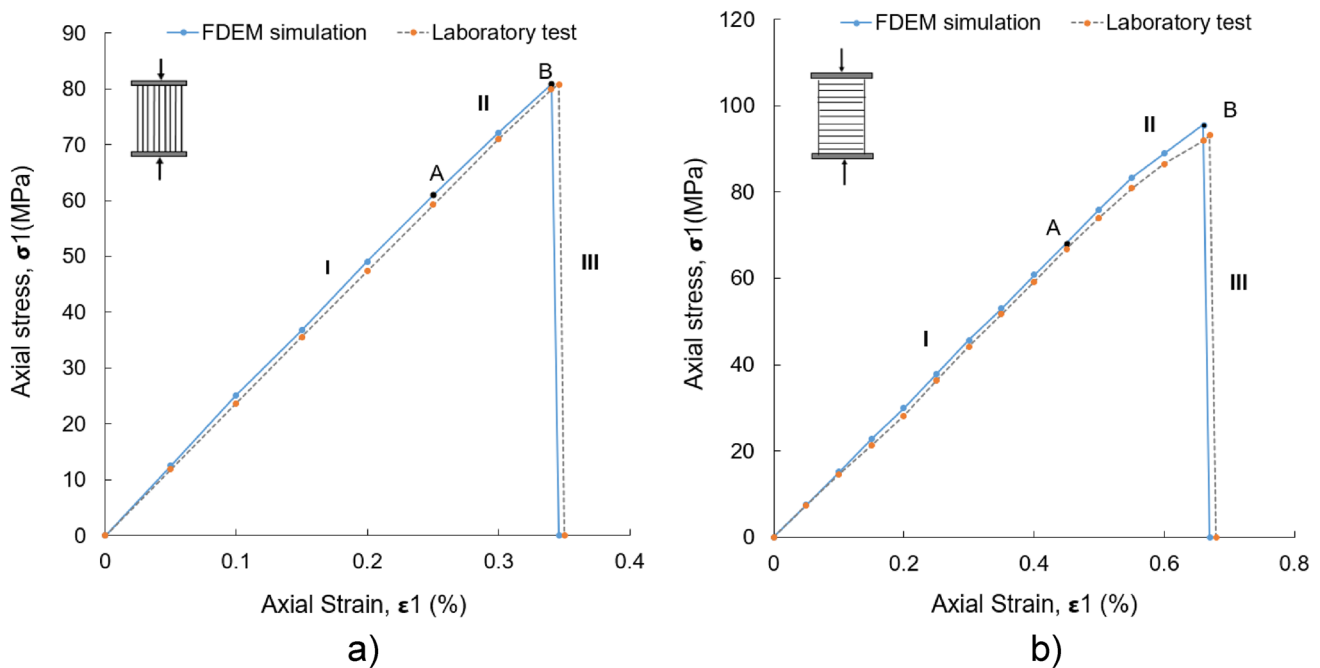
Fig. 8 The stress–strain curves of the shale for laboratory UCS test with bedding plane inclinations of **a** 90° and **b** 0°, compared with FDEM simulation results (point A is the crack damage stress threshold, and point B is the peak strength; Wang et al. 2020)

rocks (Bieniawski 1967). In the first phase, both models are linearly elastic until fractures start to form. From point 0 to point A, the FDEM model under uniaxial compression during phase I shows a linear response. The elastic response of the model is captured by the continuum of elastic elements and stiffness of the crack elements. After point A (crack damage threshold), large cracks form and coalesce inside of the model, and it leads to phase II before macro-failure of the model happens at point B. Phase III, which occurs beyond point B, is characterised by the macroscopic

fractures propagating throughout the whole model. For $\theta = 90°$ and $0°$, the uniaxial compressive strength value is 80.93 and 95.59 MPa, respectively. As shown in Table 3, these values are in good agreement with the experimental values.

Figure 9 shows how the uniaxial compressive strength and elastic modulus vary with different bedding plane inclinations, proving Longmaxi shale has apparent anisotropy. It can be seen in Fig. 9 that the uniaxial compressive strength and elastic modulus values with different bedding
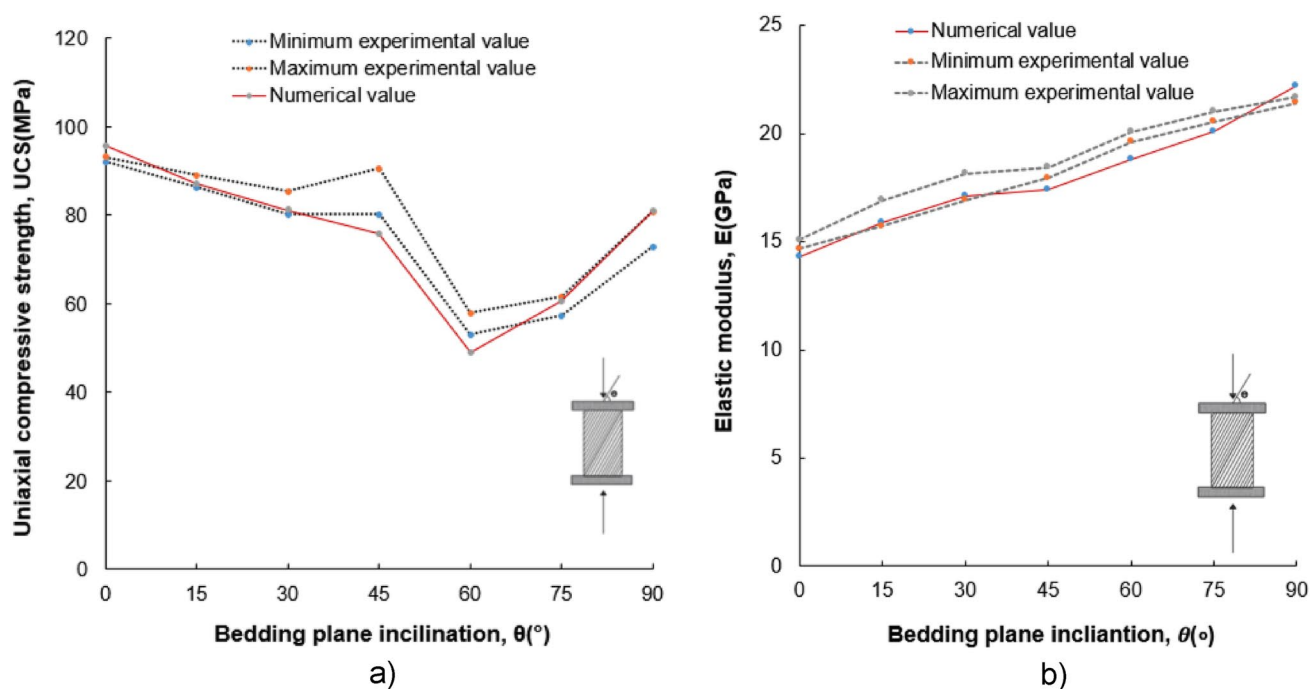
a)   b)

Fig. 9 **a** Variation of the uniaxial compressive strength and **b** elastic modulus values for the Longmaxi shale for UCS tests with different bedding plane inclinations in the FDEM models and experimental tests (Wang et al. 2020)

plane inclinations in the FDEM models coincide with the laboratory average values (Wang et al. 2020), all within 5% difference, except at 45° and 60°. While the simulation results and laboratory average values of uniaxial compressive strength at 45° and 60° differ by 9 and 7.3%, respectively, the simulation results are within 5% of the minimum laboratory values. It is the same situation with the elastic modulus. This situation may be explained by the micro-parameters of cohesive elements in the FDEM model which were calibrated against the macro-mechanical strengths of shale samples at 0° and 90°, which causes the macro-mechanical strengths of the shale FDEM models in S-M and T-S failure mode to fit better with laboratory values, as compared to B-D. As the bedding plane inclination increases, the uniaxial compressive strength initially decreases (0°–60°) and then increases, whilst Fig. 9b shows that the elastic modulus gradually increases as the bedding plane inclination increases.

Accordingly, Fig. 10 illustrates how the Poisson's ratio varies under UCS tests with different bedding plane inclinations in the FDEM model for the Longmaxi shale. Similar to the elastic modulus, the Poisson's ratio increases with increasing bedding plane inclination. This phenomenon has also been noticed by Gui et al. (2022) recently. The variation in values of the uniaxial compressive strength, elastic modulus and Poisson's ratio to different bedding plane inclinations is related to the different failure modes, which are discussed in Sect. 5.1.

4.4 Simulated Stress–Displacement Response in Brazilian Disc Tests

The indirect tensile strength, σ_t, from a BD test is calculated using Eq. (4) (Bieniawski and Hawkes 1978).

$$\sigma_t = \frac{2P_{max}}{\pi t D} \tag{4}$$

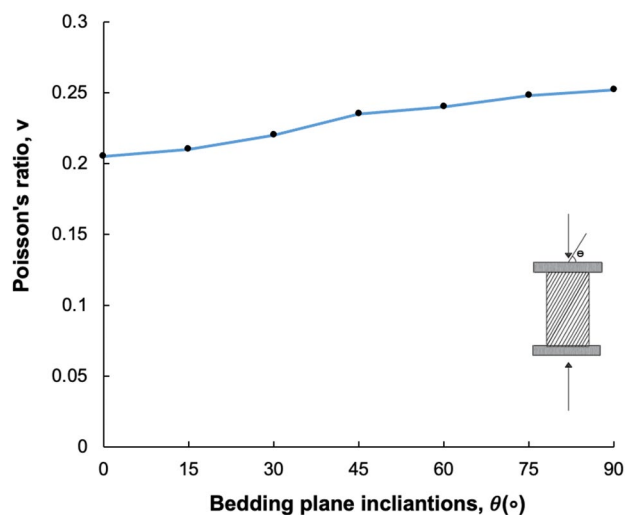**Fig. 10** Variation of the Poisson's ratio values for the Longmaxi shale for UCS tests with different bedding plane inclinations in the FDEM models

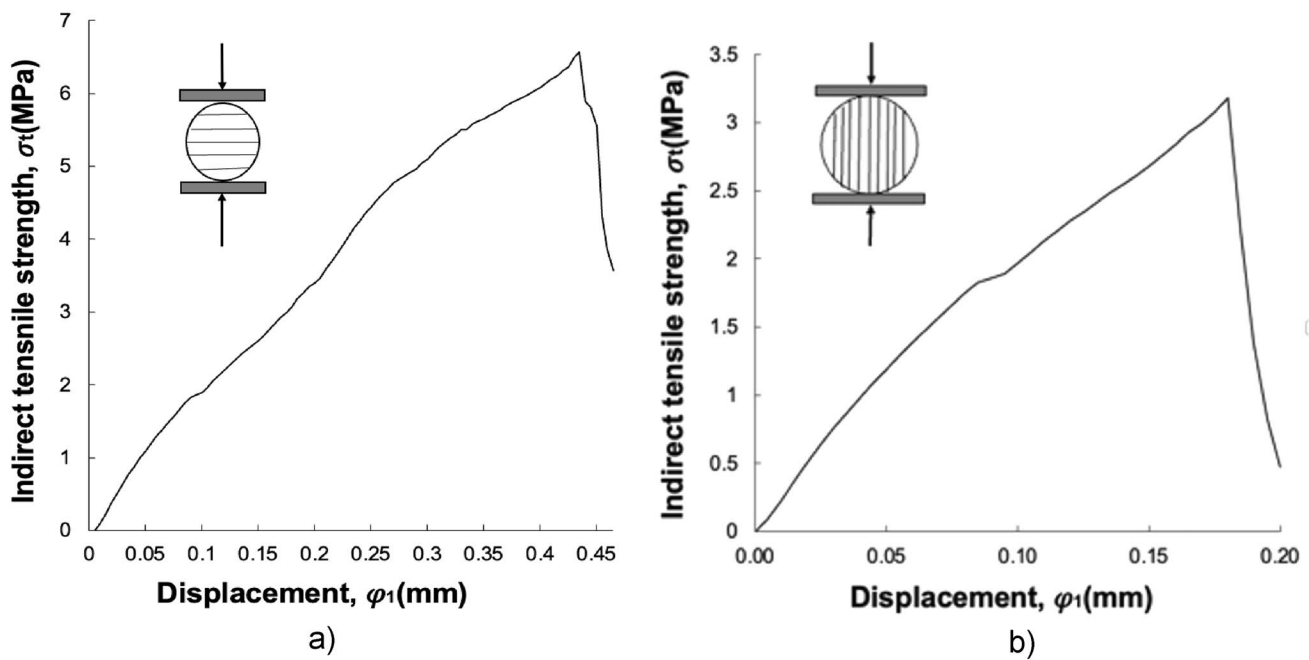**Fig. 11** Stress–displacement response of the Longmaxi FDEM model for BD tests with bedding plane inclinations at **a** 0° and **b** 90°
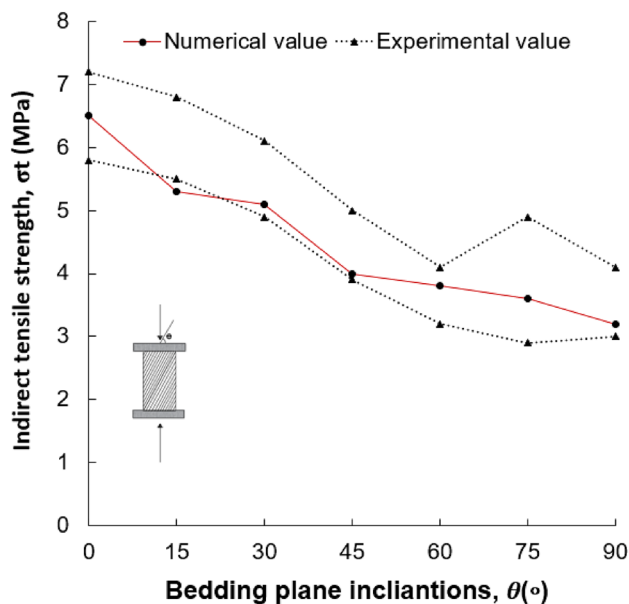

Fig. 12 Variation of the indirect tensile strength values for the Longmaxi shale for BD tests with different bedding plane inclinations in the FDEM models and experimental tests (Ma et al. 2018)

where P_{max} represents the maximum force on the loading platen, D represents the diameter of the rock sample (50 mm), and t represents the thickness of the sample (a unit thickness is assumed in 2D).

As shown in Fig. 11, the peak strength for the Longmaxi shale model with bedding plane inclinations at 0° and 90° are 6.57 and 3.17 MPa, respectively. These values match well with their respective experimental average values of 6.6 and 3.5 MPa (Table 3).

Figure 12 shows the indirect tensile strength of the experimental BD tests and the FDEM model on Longmaxi shale. As shown in Fig. 12, the indirect tensile strength values with different bedding plane inclinations in the FDEM models coincide with the laboratory tests. The two dotted lines indicate the lower and upper limits of the variation of the experiment values (Ma et al. 2018). Both the results of the experimental tests and the FDEM models indicated that the indirect tensile strength of Longmaxi shale gradually decreases as the bedding plane inclination increases.

5 Shale Failure Modes with Anisotropy

5.1 Failure Behaviour of Shale in Uniaxial Compressive Strength Test Simulations

Wang et al. (2020) collected 14 Longmaxi cylindrical specimens from Chongqing, China, with diameters of 50 mm and lengths of 100 mm. The specimens were prepared in seven directions to have seven different bedding inclinations (i.e., 0°, 15°, 30°, 45°, 60°, 75° and 90°).
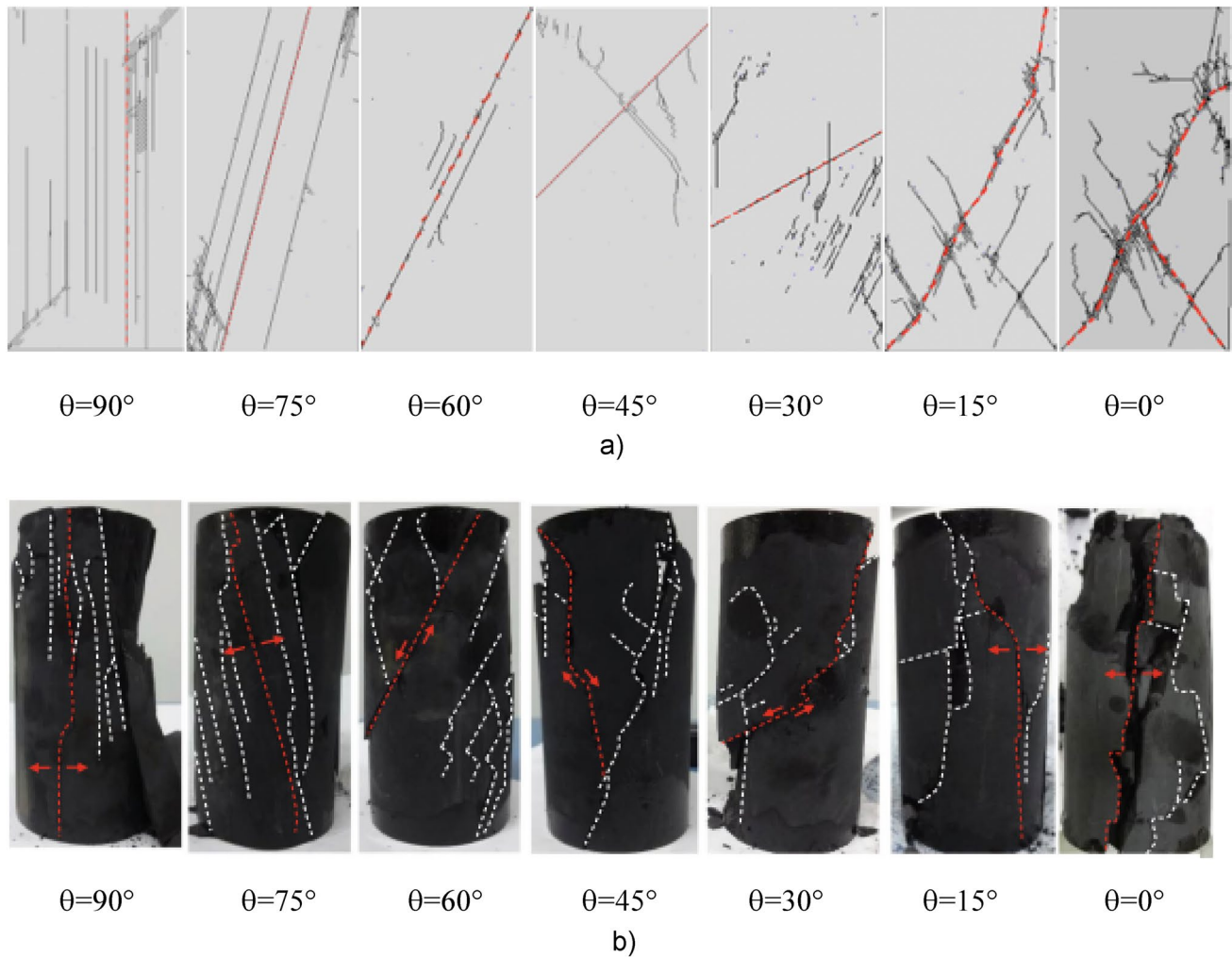
θ=90°   θ=75°   θ=60°   θ=45°   θ=30°   θ=15°   θ=0°

a)

θ=90°   θ=75°   θ=60°   θ=45°   θ=30°   θ=15°   θ=0°

b)

Fig. 13 Comparison of failure patterns during the UCS test on Longmaxi shale between FDEM models and experimental samples (the red lines indicate the main failure fractures). **a** Failure patterns of the Longmaxi FDEM model analyses with different bedding plane inclinations. **b** Failure patterns of the Longmaxi laboratory specimens with different bedding plane inclinations (Wang et al. 2020)

Each inclination was repeated twice. Fig. 13 illustrates the failure of shale specimens with different orientations under UCS tests in both simulations and experimental tests. The macroscopic failure response of the Longmaxi shale observed in the FDEM model and experimental tests (Fig. 13a, b) highlights a distinct variation in the failure patterns depending on the bedding plane inclination.

As shown in Fig. 13a, b, the failure modes of the shale with different bedding plane inclinations can be classified into three distinct modes, with transition phases between these modes. For a shale with larger bedding plane inclinations (90° and 75°), the failure of the shale is caused by tensile splitting (T-S) along the bedding planes. Multiple tensile fractures developed through the bedding planes, while some shear fractures formed between the layers. For plane inclination values from 30° to 60°, the failure mode of the shale

involved bedding plane delamination (B-D). This generally involved two major types of fractures: major fractures shearing along the bedding plane and tensile fractures forming perpendicular to the shearing fractures. For shale with bedding plane inclinations from 0° to 15°, the specimens failed due to cracks shearing through the rock matrix (S-M).

When the shale is in the T-S mode, the fractures extend along the bedding planes. The tensile splitting of the failed shale specimen leads to circumferential expansion. In this case, there is a small deformation along the vertical axis of the specimen indicating that shale under T-S has larger elastic modulus values. For shale in the B-D failure mode, shale models tend to shear along bedding planes. This plane works as the weakest plane in the shale, which results in the lowest uniaxial compressive strength values, as shown in Fig. 9a. This observation agrees with the conventional Coulomb-Navier theory that the

weakest plane for shale under compression is approximately given by Eq. (5) (Lisjak et al. 2014).

$$\alpha = 45° - \frac{1}{2}\phi_i \tag{5}$$

where ϕ_i is the rock internal friction angle and α is the angle between the failure plane and the maximum principal stress. Due to the change in failure mode from T-S to B-D, the shale specimens show more axial deformation, which leads to a smaller elastic modulus, as shown in Fig. 9b. When the shale is in the S-M mode, the strength of the shale matrix plays a dominant role in controlling the failure strength of the shale specimens as the fractures form inside of the matrix. In this case, the shale failure strength in the S-M mode is larger than for the other two modes. Compared to fracturing along the bedding plane in mode B-D, a shale matrix with larger strength allows the shale specimens to have a larger deformation (including elastic and plastic) along the vertical axis in the S-M mode; consequently, the S-M mode has the smallest elastic modulus, compared with the other two failure modes.

5.2 Failure Behaviour of Shale in Brazilian Disc Test Simulations

The failure modes of all the FDEM model analyses and experimental tests are displayed in Fig. 14a and b, respectively. Three different modes can be distinguished from the results, which indicates that the shale bedding plane inclination significantly influences the anisotropic strength of the shale. As shown in Fig. 14a, b, the three different failure modes can be described as: (1) central spilt along the bedding planes (C-S) when $\theta = 90°$ and $75°$; (2) inclined arch fracturing (I-A) when $\theta = 60°$, $45°$ and $30°$; (3) central arch fracturing (C-A) with branches when $\theta = 15°$ and $0°$. The ranges of q between these classified modes show transitional fracture patterns with no clear threshold between the modes. When the shale is in the C-A failure mode, fractures are mainly formed through the shale matrix, which leads to a greater tensile strength than other modes (Fig. 12). With an increase in bedding plane inclination, more fractures form along the bedding planes as these provide weaker pathways for the fractures to propagate. In turn, the tensile strength of the shale decreases gradually, as shown in Fig. 12.
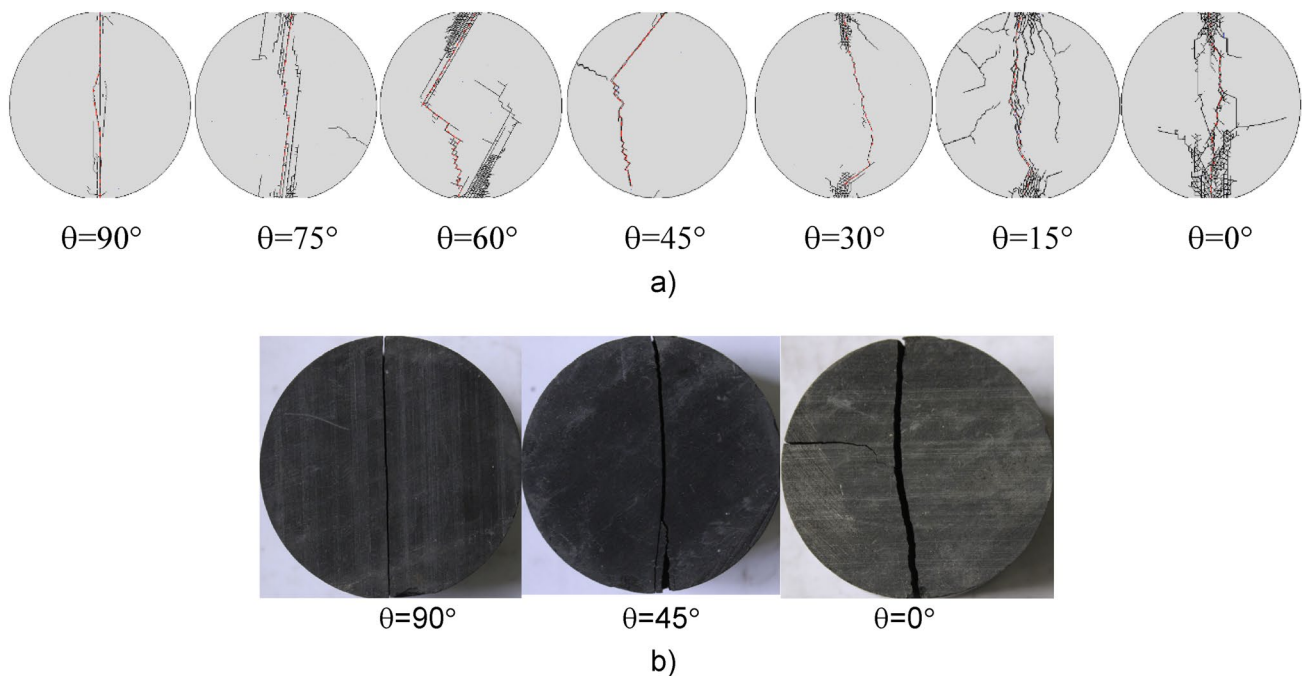

$\theta=90°$ $\theta=75°$ $\theta=60°$ $\theta=45°$ $\theta=30°$ $\theta=15°$ $\theta=0°$

a)

$\theta=90°$ $\theta=45°$ $\theta=0°$

b)

Fig. 14 Comparison of the failure patterns during BD tests on Longmaxi shale **a** FDEM model results and **b** experimental test specimens (Heng et al. 2020).
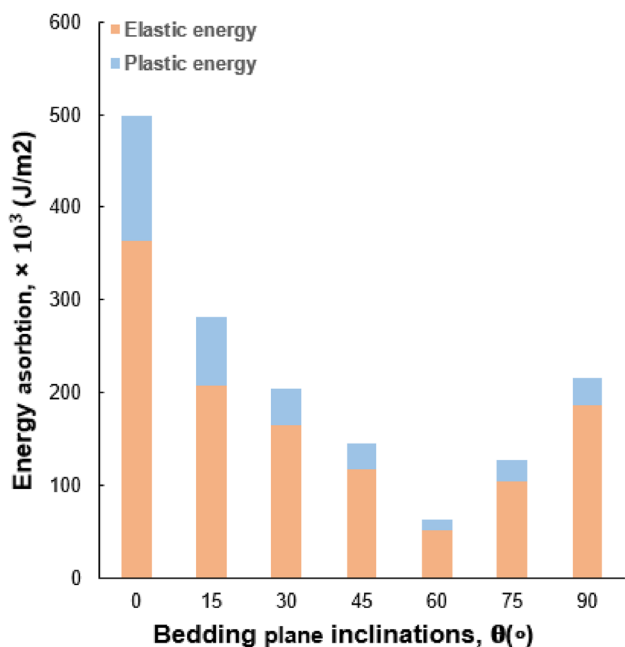
Fig. 15 The absorption of energy pre-failure

Fig. 16 Variation in brittleness indices ($BI_{4\text{-}E}$, $BI_{4\text{-}S}$, $BI_{5\text{-}E}$ and $BI_{5\text{-}S}$) with bedding plane inclinations

6 Shale Brittleness with Anisotropy

6.1 Analysis of Conventional Brittleness Indices for Longmaxi shale

As the stress–strain curve of rock can be quickly obtained from the conventional UCS or triaxial compression tests, a brittleness index based on the stress–strain curve has been commonly adopted in previous research to characterise the relative behaviour of materials (Hucka and Das 1974; Li et al. 2017). This paper only discusses fractures forming inside shale samples before macro-failure; therefore, BI_4 and BI_5 (from Table 1), based on the stress–strain curve before the pre-peak phase, have been applied to evaluate the brittleness of the Longmaxi shale. The BI_5 index based on the energy evolution prior to failure is given by Eq. (6) (Munoz et al. 2016).

$$BI_5 = \frac{U_{et}}{U_t} = \frac{\sigma_u 2}{2E \int_0^{\epsilon_u} \sigma d\epsilon} \tag{6}$$

From Eq. (6), the brittleness index ranges from 0 to 1, with a larger BI indicating greater brittleness.

From the stress–strain curves of different shale analyses with different bedding plane inclinations, the value of the energy absorption can be obtained using Eqs. (1) and (2), which is shown in Fig. 15. This figure indicates that the energy absorption in shale shows anisotropic properties with bedding plane inclination. The shape of the curve between the energy absorption and the bedding plane inclination is
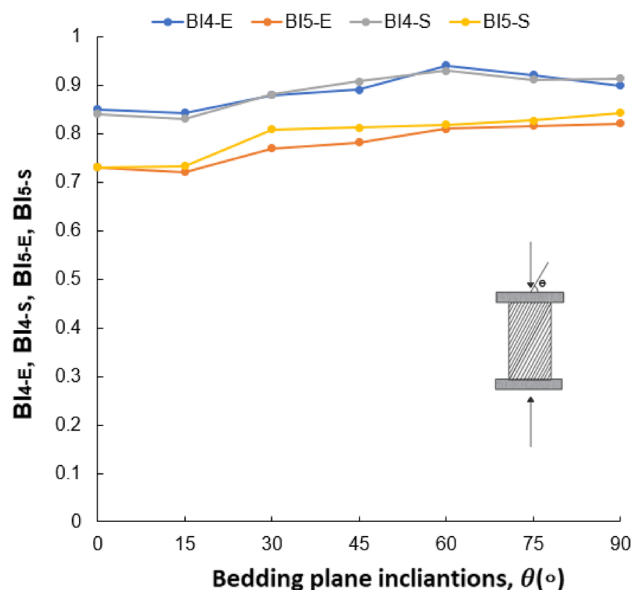
the same as the uniaxial compressive strength, which is a 'U' shape. The uniaxial compressive strength has a significant effect on the energy absorption. Initially, the absorbed energy decreases as the bedding plane inclination increases from 0° to 60°. After the value of the absorbed energy reaches a minimum value at 60°, it starts to increase with increasing bedding plane inclination. From the last section, it was shown that shale failure can be divided into three modes associated with different bedding plane inclinations, i.e., T-S between 0° and 15°, B-D between 30° and 60° and S-M between 75° and 90°. The shale in the S-M failure mode needs more energy to reach macro-failure when compared to other modes. This can be attributed to the bedding plane being weaker than the matrix. Once damage occurs along the bedding plane, fractures form and propagate quickly, which leads to smaller plastic deformations and lower energy dissipation.

Figure 16 shows the variation in conventional brittleness indices, in terms of $BI_{4\text{-}S}$, $BI_{4\text{-}E}$, $BI_{5\text{-}S}$ and $BI_{5\text{-}E}$, with different bedding plane inclinations. Simulation-derived $BI_{4\text{-}S}$ and $BI_{5\text{-}S}$ brittleness indices for BI_4 and BI_5 are compared with experimentally-derived $BI_{4\text{-}E}$ and $BI_{5\text{-}E}$ brittleness indices for BI_4 and BI_5 (Wang et al. 2018a, b; 2020). As shown in Fig. 16, BI_4 and BI_5 show similar (within a maximum 4% relative error for BI_5 at 30°, and within an average 1% relative error for BI_4 and 1.9% relative error for BI_5) experimental and simulation trends in the data. The curves of BI_4 and BI_5 indicate that the bedding plane inclinations have a large influence on the brittleness of shale. For BI_4 and BI_5, the brittleness index of the three modes in magnitude order is T-S > B-D > S-M. When the inclination of the bedding plane
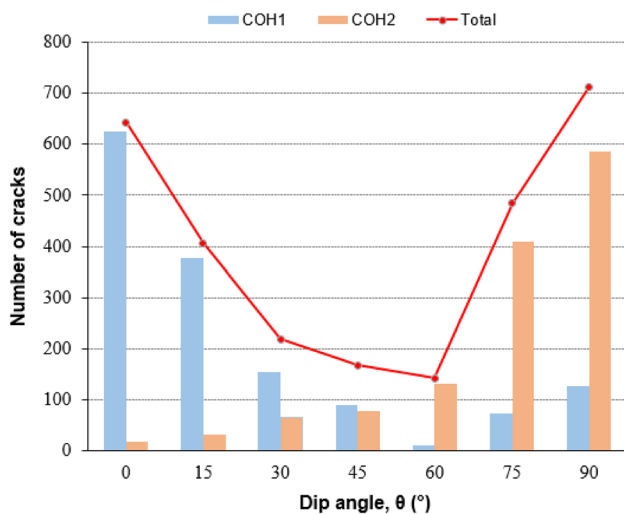
Fig. 17 Failed cohesive elements inside the shale with bedding plane inclination

increases from 0° to 30°, the failure mode changes from S-M to B-D. As the shale matrix is stronger, shale in the S-M mode can provide enough plastic deformation, which leads to more energy dissipation. As the fractures propagate more easily along the bedding planes, the shale will become more brittle. Therefore, the brittleness in the B-D mode is larger than in the S-M mode. In contrast, compared to splitting, shear failure tends to occur by slippage along the bedding plane, which allows for larger plastic deformation and lower brittleness. Overall, the brittleness values of the three failure modes of shale with different bedding plane inclinations are in the order: T-S > B-D > S-M.

6.2 New Proposed Brittleness Indices

6.2.1 New Brittleness Index BI_f

During the energy dissipation of the pre-peak phase, a proportion of the energy is consumed by fractures forming and propagating. According to previous research, it is assumed that rock materials with higher values of brittleness are more prone to form fractures (Cotterell and Rice 1980). The number of cracks generated inside the FDEM models before macro-failure for different bedding plane inclinations are shown in Fig. 17. The largest number of fractures formed in the shale with a bedding plane inclination of 90°, while the shale with a bedding plane inclination of 60° has the smallest value. Shale with a bedding plane inclination of 0° has the smallest brittleness indices, however, it has a large number of cracks. This can be explained by the energy dissipation. From Fig. 15, the shale with a 0° bedding plane inclination has consumed the largest energy due to the internal damage, which is because of the large plastic deformation.

However, even though the value of energy dissipation at 0° is approximately four times larger than at 90°, the number of cracks that form is similar. It is understood that fracturing within the matrix needs more energy than failure along bedding planes, and multiple fractures tend to form at the same time along the bedding planes in the T-S failure mode. Thus, although the shale with plane inclinations of 0° and 15° have a larger plastic energy compared to 75° and 90°, the number of cracks is smaller. Meanwhile, shale in the B-D failure mode tends to form and propagate along one or limited bedding planes, which leads to a smaller number of fractures. Overall, the number of total fractures formed inside the shale for the three failure modes are in the order: T-S > S-M > B-D. Meanwhile, the number of fractures forming along the bedding plane (COH2) is smaller than the number of fractures in the shale matrix (COH1) in the T-S failure mode, as shown in Fig. 17. As the fractures mainly form and propagate along the bedding plane in shale with bedding plane inclinations of 60°, COH2 has the greatest frequency compared to other bedding plane inclinations. Fractures tend to form inside the matrix as the bedding plane inclinations decrease, which leads to an increase in the frequency of COH1. As a result, the S-M failure mode consumes more energy than the other two failure modes.

According to Fig. 17, a higher brittleness based on conventional brittleness indices did not show a higher number of fractures. From the above discussion, it can be deduced that shale in the S-M failure mode has a large plastic deformation, which leads to a larger plastic energy. This larger plastic energy can provide enough energy for the formation of fractures. Therefore, looking at the total fractures to evaluate the brittleness of the rock may not be the best way to present the brittleness of shale. However, understanding the brittleness of the rock to predict the evolution of fractures in shale is necessary. Therefore, a new brittleness index BI_f is proposed in this study given in Eq. (7):

$$BI_f = \frac{M}{U_P} \tag{7}$$

where M is the total number of fractures formed in the pre-peak phase, and U_P is the plastic energy. The details of crack formation (e.g., fracture number) in the laboratory tests can be gained from X-ray computed tomography (CT) images and acoustic emission (AE) (Wang et al. 2016a, b; Zhai et al. 2020). The fracture number in rocks during uniaxial compressive tests can be estimated by analysing the AE events during compression (Lisjak et al. 2013; Chen et al. 2021). BI_f should be corroborated with experimental tests in future work. However, capturing the fracture number in AE needs to be done carefully as there could be a discrepancy in fracture number between the experiments and FDEM models caused by mesh size in the model. To corroborate the

Fig. 18 The variation in BI_f with different bedding plane inclinations
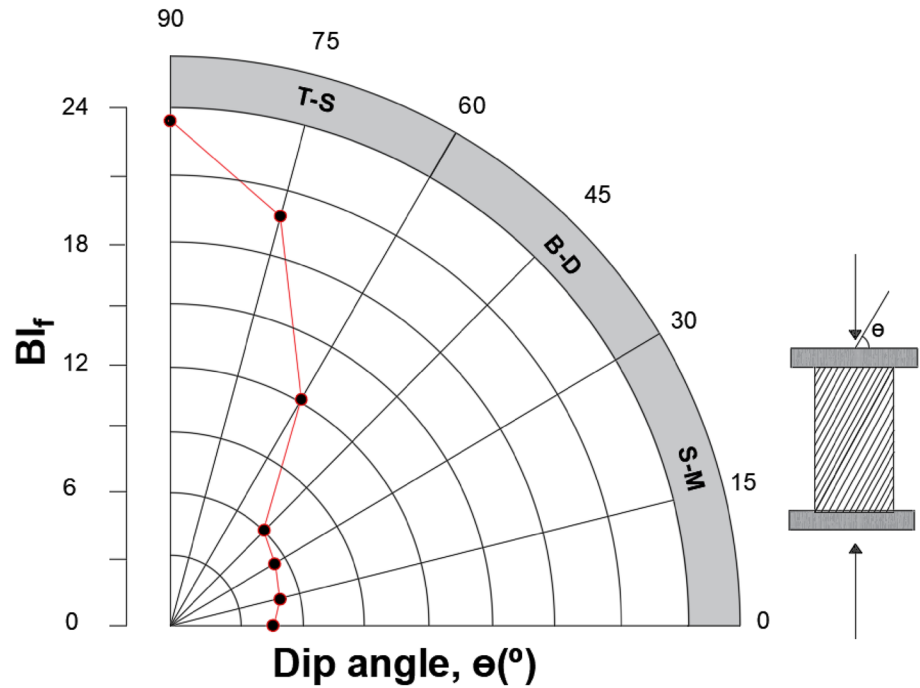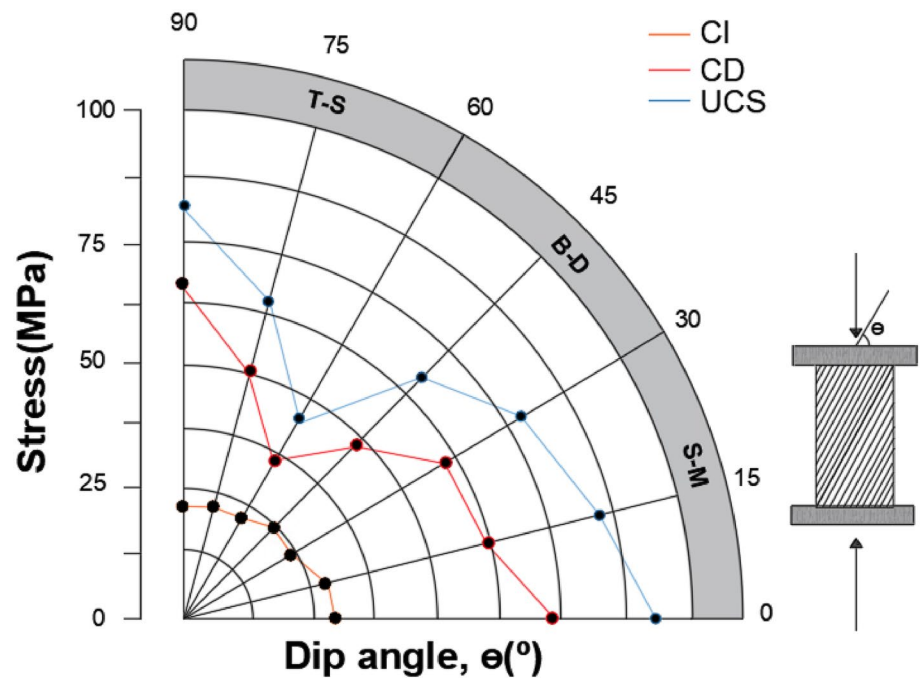

Fig. 19 Uniaxial compressive strength, CI and CD variation with different bedding plane inclinations

simulated fracture number, the amplitude threshold of AE events in laboratory tests should correspond to the kinetic energy of a single crack element during failure in the FDEM model. This brittleness index indicates the number of fractures formed per unit of energy dissipation. This brittleness index indicates the ability of the shale to transform energy into fractures, with a higher brittleness index indicating the shale is more likely to form fractures.

Figure 18 indicates that as the bedding plane inclination increases, the BI_f increases, and hence the number of fractures formed per unit energy dissipation also increases. The transfer of energy to fractures in the three failure modes of the shale are in the order: T-S > B-D > S-M.

In the three failure modes of the shale under different bedding plane inclination, the brittleness indices BI_4, BI_5

and BI_f have revealed that the order of the brittleness for the three failure modes is T-S > B-D > S-M.

6.2.2 New Brittleness Index BI_{CD}

Crack initiation stress (CI) is defined as the stress threshold at which cracks start forming and propagating, whereas crack damage stress (CD) is defined as the stress level where cracks start to form unstably and coalesce into a major fracture. Figure 19 depicts that the impact of shale anisotropy on CI is limited. It can be noticed that the CIs for different bedding inclinations are close to the average value (25.19 MPa). With a 0° bedding plane inclination, the maximum difference between the average value and the CI is 1.97 MPa, which differs by approximately 7.8% from the average value. CD, however, shows a large variation for the different bedding plane inclinations, indicating CD is also sensitive to bedding plane inclination, as is UCS. When the stress inside the shale reaches the CI under the UCS test, cracks begin to form and propagate inside the shale. They may propagate along the bedding plane, cross the bedding plane, or even stop propagating, which depends on the bedding plane inclination. Different crack paths lead to different strains and stresses within the shale, which leads to different thresholds of the CD and failure patterns.

Based on this observation, a new brittleness index, BI_{CD} is proposed in this study as shown in Eq. (8).

$$BI_{CD} = CD/\sigma_u \qquad (8)$$

As with the other brittleness indices, the higher the value of BI_{CD}, the more brittle the shale. The variation of BI_{CD} based on the Longmaxi shale FDEM modelling with different bedding plane inclinations is shown in Fig. 20. The order of the BI_{CD} for the three failure modes is T-S > B-D > S-M. With increasing bedding plane inclination, the higher the value of BI_{CD}, which agrees with BI_4, BI_5 and BI_f. This behaviour is due to brittle rocks having a smaller plastic deformation (Gong et al. 2022). The higher the value of BI_{CD}, the quicker the rock reaches the σ_u after the threshold of CD with smaller plastic strains.

7 New Empirical Relationship to Predict Tensile Stress Based on UCS Test

Compared to the conventional brittleness index BI_2, based on the σ_u and σ_t ratio, BI_{CD} is easier to obtain as it only requires the UCS test to be performed. To validate the accuracy of BI_{CD}, values of BI_{CD} collected from different rock types (obtained from the published literature) are plotted in Fig. 21. It can be seen from Fig. 21 that there is an apparent trend between BI_{CD} and BI_2. Based on the rock data presented in Fig. 21, there are minimum values of BI_{CD} and BI_2 of 0.58 and 6.47, respectively. Due to the ease of obtaining BI_{CD} compared to other brittleness indices, it can be a useful

Fig. 20 Variation of BI$_{CD}$ based on the Longmaxi shale FDEM models with different bedding plane inclinations
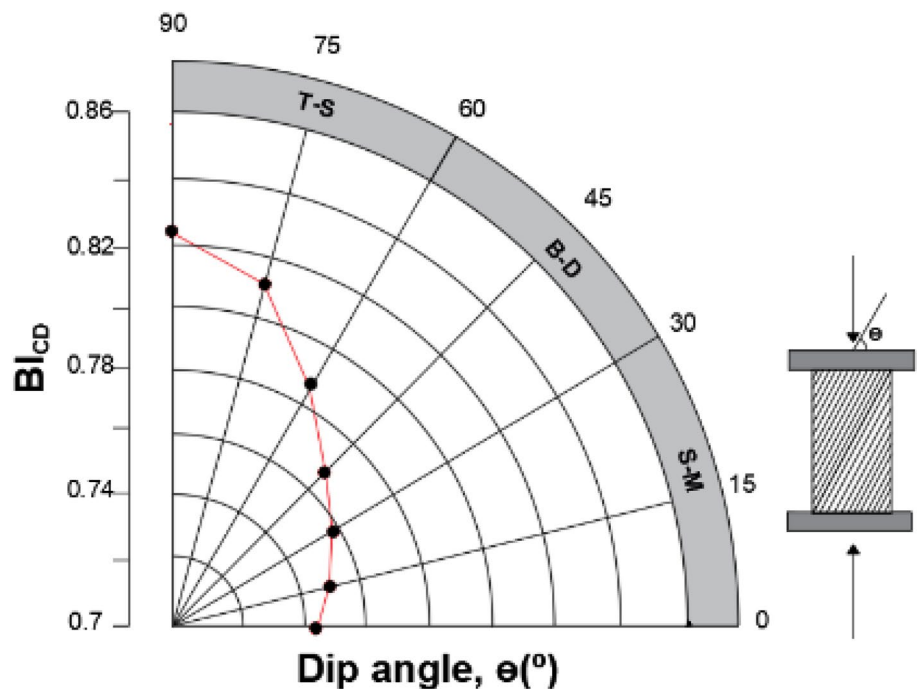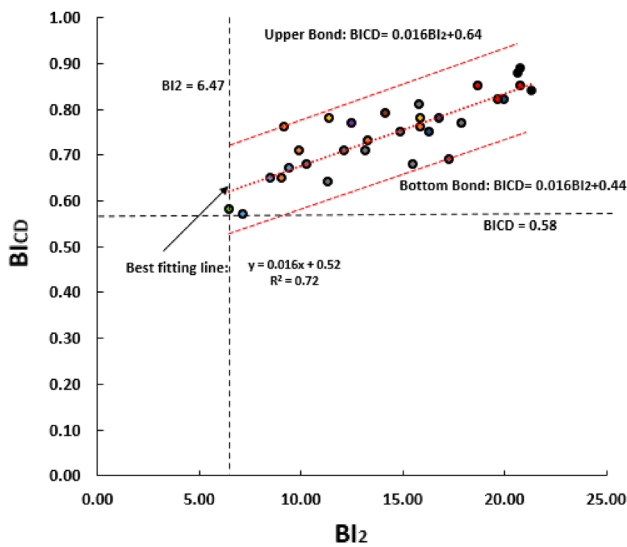
Fig. 21 BI_{CD} vs. BI_2 for different rocks, including granite (red), shale (grey), limestone (orange), diorite (dark blue), siltstone (green), sandstone (blue), coal (yellow), marble (black) and quartzites (brown) (Xue et al. 2014; Cai et al. 2004; Ghasemi et al. 2020; Palchik and Hatzor 2002; Li et al. 2020; Zhao et al. 2013; Modiriasari et al. 2017; Gatelier et al. 2002; Palchik 2010; Wu et al. 2021; Taheri et al. 2020; Song et al. 2020a, b; Wang et al. 2016a, b)

way of predicting the brittleness of different rocks, including shales.

Figure 21 shows the relationship between the BI_2 and BI_{CD} obtained from different laboratory samples, which fits between the upper bound: $BI_{CD}=0.016BI_2+0.64$ and lower bound: $BI_{CD}=0.016BI_2+0.44$. BI_2 is the ratio between the σ_u and σ_t, while BI_{CD} is the ratio between the CD and σ_u, with the upper bound written as: $BI_{CD}=0.016\frac{\sigma_u}{\sigma_t}+0.64$, and the lower bound is: $BI_{CD}=0.016\frac{\sigma_u}{\sigma_t}+0.44$. The empirical equations for the upper line and bottom line indicate that there is a relationship between the tensile strength and CD. The relationship between σ_t and CD based on the upper and lower fitted lines is:

$$\sigma_{t_{min}} = \frac{0.016\sigma_u}{\frac{CD}{\sigma_u} - 0.44} < \sigma_t < \sigma_{t_{max}} = \frac{0.016\sigma_u}{\frac{CD}{\sigma_u} - 0.64} \qquad (9)$$

where σ_u is the uniaxial compressive strength, CD is the crack damage stress and σ_t is the tensile strength. In Fig. 22, the predicted tensile strength for the Longmaxi shale with different bedding plane inclinations using Eq. (9) is compared with the experimental values showing that these are in line with the predicted range of tensile strength values using Eq. (9). Considering that testing the tensile strength of rocks may be difficult under certain conditions, using the empirical relationships (Eq. 9) to predict the range of the tensile strength of the rock may provide a useful alternative method.
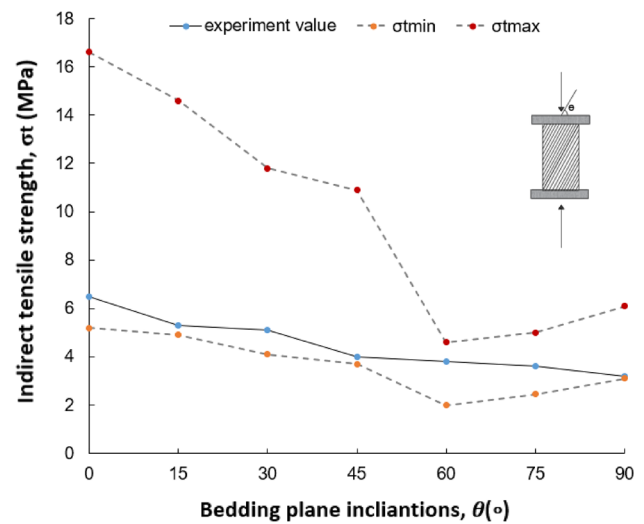

Fig. 22 The comparisons between the predicted tensile strength for shale with different bedding plane inclinations using the empirical relationships and the experimental values (Ma et al. 2018)

8 Conclusions

A new modelling method has been used to create anisotropic shale models based on FDEM to study the anisotropic behaviour of Longmaxi shale from a microscopic level through a Python code-based ABAQUS model. In comparison to conventional continuum methods, FDEM has shown it can capture the failure mode of rocks by simulating fracture formation and propagation, which has brought new insight into the behaviour of the shale anisotropy properties from a micro-crack level. The key conclusions are:

(1) Three failure modes were identified from both the numerical models and published experimental results in the UCS test which are S-M ($\theta=0°$ and 15°), B-D ($\theta=30°$, 45° and 60°) and T-S ($\theta=75°$ and 90°), with transitioning phases between these. Meanwhile, failure modes of shale in BD tests can be recognised into three different modes: C-S ($\theta=75°$ and 90°), I-A ($\theta=30°$, 45° and 60°), C-A ($\theta=0°$ and 15°).

(2) The brittleness of shale is greatly affected by the shale anisotropy. Based on conventional brittleness indices obtained from both experimental and simulation results, the brittleness for the three failure modes of shale with different bedding plane inclinations is in the order: T-S > B-D > S-M.

(3) The total number fractures of shale under stress in the UCS test is not only related to the brittleness or fracability of shale, but also shale structures. High brittleness in shale means it is more easily fractured, as it has greater frac-ability. However, the total number

of fractures formed inside the shale for the three failure modes are in the order: T-S > S-M > B-D. The total fracturing number of shale under stress is related to the shale structure, as it significantly affects the fracturing paths.

(4) The anisotropic property of shale significantly affects the mechanical strength and failure mechanism at micro-crack level. The CD threshold obtained from the UCS test on shale with different bedding plane inclinations shows sensitivity to shale anisotropic properties. The reason is that the CD corresponds closely to crack propagation, and different bedding layer orientations will affect crack propagation paths.

(5) Two new brittleness indices were proposed in this study to improve the brittleness evaluation of shale. BI_f, based on rock energy evolution, to predict the fracture formation inside the shale is proposed. The BI_f describes the efficiency of shale to transform plastic energy into fractures under compression. A better understanding of a rock's frac-ability during tunnelling projects constructed in highly anisotropic shale can inform practitioners of the self-supporting capability of the rock mass and thus the required lining and support design. The proposed brittleness index, BI_f, while not evaluated at a large scale yet, has the potential to provide the fracturing conditions of the surrounding rock due to tunnel excavation. Meanwhile, BI_{CD}, based on the ratio between the CD and the uniaxial compressive strength, has been proven by both experimental data and numerical simulation data to be able to accurately evaluate shale brittleness. Comparing BI_{CD} to conventional brittleness indices, based on the ratio between uniaxial compressive strength and tensile strength, BI_{CD} can be easily gained from the UCS test, which makes it more convenient for evaluating the brittleness of rocks. BI_{CD} and BI_f for the three modes are in the same order: T-S > B-D > S-M.

(6) An empirical relationship has been proposed to predict the tensile strength based on the UCS tests. It has been shown that there is a relationship between the tensile strength and CD. Considering that directly obtaining the tensile strength of rocks may be difficult under certain conditions, using this empirical relationship based only on the UCS test can provide an alternative. However, this empirical relationship needs further evaluation (e.g., more experimental data on different types of rocks) to give greater confidence in its accuracy. In addition, this general relationship only covers a certain range of tensile strength.

Declarations

References

Abousleiman Y, Tran M, Hoang S, Bobko C, Ortega A, Ulm FJ (2007) November. Geomechanics field and laboratory characterization of Woodford shale: the next gas play. In: SPE Annual Technical Conference and Exhibition. OnePetro

Ai C, Zhang J, Li YW, Zeng J, Yang XL, Wang JG (2016) Estimation criteria for rock brittleness based on energy analysis during the rupturing process. Rock Mech Rock Eng 49(12):4681–4698

Ali E, Guang W, Weixue J (2014) Assessments of strength anisotropy and deformation behavior of banded amphibolite rocks. Geotech Geol Eng 32(2):429–438

Amadei B (1996) Importance of anisotropy when estimating and measuring in situ stresses in rock. Int J Rock Mech Min Sci Geomech Abstracts 33(3):293–325

Bai M (2016) Why are brittleness and fracability not equivalent in designing hydraulic fracturing in tight shale gas reservoirs. Petroleum 2(1):1–19

Bieniawski ZT (1967) Mechanism of brittle fracture of rock: part I—theory of the fracture process. Int J Rock Mech Min Sci Geomech Abstracts 4(4):395–406

Bieniawski ZT, Hawkes I (1978) Suggested methods for determining tensile strength offshore rock materials. Int J Rock Mech Min Sci 15:99–103

Bishop AW (1971) The influence of progressive failure on the choice of the method of stability analysis. Geotechnique 21(2):168–172

Bonnelye A, Schubnel A, David C, Henry P, Guglielmi Y, Gout C, Fauchille AL, Dick P (2017) Strength anisotropy of shales deformed under uppermost crustal conditions. J Geophys Res Solid Earth 122(1):110–129

Cai M, Kaiser PK, Tasaka Y, Maejima T, Morioka H, Minami M (2004) Generalized crack initiation and crack damage stress thresholds of brittle rock masses near underground excavations. Int J Rock Mech Min Sci 41(5):833–847

Cao H, Gao Q, Ye G, Zhu H, Sun P (2020) Experimental investigation on anisotropic characteristics of marine shale in Northwestern Hunan, China. J Nat Gas Sci Eng 81:103421

Chandler MR, Meredith PG, Brantut N, Crawford BR (2016) Fracture toughness anisotropy in shale. J Geophys Res Solid Earth 121(3):1706–1729

Chandra N, Li H, Shet C, Ghonem H (2002) Some issues in the application of cohesive zone models for metal–ceramic interfaces. Int J Solids Struct 39(10):2827–2855

Chen B, Xiang J, Latham JP, Bakker RR (2020) Grain-scale failure mechanism of porous sandstone: an experimental and numerical FDEM study of the Brazilian Tensile Strength test using CT-Scan microstructure. Int J Rock Mech Min Sci 132:104348

Chen Y, Xu J, Peng S, Jiao F, Chen C, Xiao Z (2021) Experimental study on the acoustic emission and fracture propagation characteristics of sandstone with variable angle joints. Eng Geol 292:106247

Cotterell B, Rice J (1980) Slightly curved or kinked cracks. Int J fracture 16:155-169

Cundall PA (1971) A computer model for simulating progressive large scale movements in blocky system. In: Proc. Int. Symp. on Rock Fractures, p. II-8

Deng P, Liu Q, Huang X, Bo Y, Liu Q, Li W (2021) Sensitivity analysis of fracture energies for the combinedfinite-discrete element method (FDEM). Eng Fracture Mech 251:10779

Doležalová M (2001) Tunnel complex unloaded by a deep excavation. Comput Geotech 28(6–7):469–493

Duan K, Kwok CY, Tham LG (2015) Micromechanical analysis of the failure process of brittle rock. Int J Numer Anal Methods Geomech 39(6):618–634

Fabre G, Pellet F (2006) Creep and time-dependent damage in argillaceous rocks. Int J Rock Mech Min Sci 43(6):950–960

Fjær E, Nes OM (2014) The impact of heterogeneity on the anisotropic strength of an outcrop shale. Rock Mech Rock Eng 47(5):1603–1611

Fukuda D, Liu H, Zhang Q, Zhao J, Kodama JI, Fujii Y, Chan AHC (2021) Modelling of dynamic rock fracture process using the finite-discrete element method with a novel and efficient contact activation scheme. Int J Rock Mech Min Sci 138:104645

Gatelier N, Pellet F, Loret B (2002) Mechanical damage of an anisotropic porous rock in cyclic triaxial tests. Int J Rock Mech Min Sci 39(3):335–354

Geng Z, Chen M, Jin Y, Yang S, Yi Z, Fang X, Du X (2016) Experimental study of brittleness anisotropy of shale in triaxial compression. J Nat Gas Sci Eng 36:510–518

Ghaboussi J, Wilson EL, Isenberg J (1973) Finite element for rock joints and interfaces. J Soil Mech Found Div 99(10):833–848

Ghasemi S, Khamehchiyan M, Taheri A, Nikudel MR, Zalooli A (2020) Crack evolution in damage stress thresholds in different minerals of granite rock. Rock Mech Rock Eng 53(3):1163–1178

Gong F, Zhang P, Du K (2022) A novel staged cyclic damage constitutive model for brittle rock based on linear energy dissipation law: modelling and validation. Rock Mech Rock Eng 55(10):6249–6262

Goodman RE (1968) A model for the mechanics of jointed rock. J Soil Mech Found Div 94:637–659

Gui J, Guo J, Sang Y, Chen Y, Ma T, Ranjith PG (2022) Evaluation on the anisotropic brittleness index of shale rock using geophysical logging. Petroleum. https://doi.org/10.1016/j.petlm.2022.06.001

Hakala M, Kuula H, Hudson JA (2007) Estimating the transversely isotropic elastic intact rock properties for in situ stress measurement data reduction: a case study of the Olkiluoto mica gneiss, Finland. Int J Rock Mech Min Sci 44(1):14–46

Hammah RE, Yacoub T, Corkum B, Curran JH (2008) The practical modelling of discontinuous rock masses with finite element analysis. In: The 42nd US Rock Mechanics Symposium (USRMS). OnePetro

Hao XJ, Feng XT, Yang CX, Jiang Q, Li SJ (2016) Analysis of EDZ development of columnar jointed rock mass in the Baihetan diversion tunnel. Rock Mech Rock Eng 49(4):1289–1312

He B, Liu J, Zhao P, Wang J (2021) PFC2D-based investigation on the mechanical behavior of anisotropic shale under Brazilian splitting containing two parallel cracks. Front Earth Sci 15:803–816

Heng S, Li X, Liu X, Chen Y (2020) Experimental study on the mechanical properties of bedding planes in shale. J Nat Gas Sci Eng 76:103161

Hoek E, Brown ET (1980) Empirical strength criterion for rock masses. J Geotech Eng Div 106(9):1013–1035

Huang LC, Xu ZS, Zhou CY (2009) Modeling and monitoring in a soft argillaceous shale tunnel. Acta Geotech 4(4):273

Hucka V, Das B (1974) Brittleness determination of rocks by different methods. Int J Rock Mech Min Sci Geomech Abstracts 11(10):389–392

Ivars DM, Pierce ME, Darcel C, Reyes-Montes J, Potyondy DO, Young RP, Cundall PA (2011) The synthetic rock mass approach for jointed rock mass modelling. Int J Rock Mech Min Sci 48(2):219–244

Jaeger JC (1960) Shear failure of anistropic rocks. Geol Mag 97(1):65–72

Jarvie DM, Hill RJ, Ruble TE, Pollastro RM (2007) Unconventional shale-gas systems: the Mississippian Barnett Shale of north-central Texas as one model for thermogenic shale-gas assessment. AAPG Bull 91(4):475–499

Jiang G, Zuo J, Li Y, Wei X (2019) Experimental investigation on mechanical and acoustic parameters of different depth shale under the effect of confining pressure. Rock Mech Rock Eng 52:4273–4286

Kasyap SS, Senetakis K (2022) Characterization of two types of shale rocks from Guizhou China through micro-indentation, statistical and machine-learning tools. J Petrol Sci Eng 208:109304

Keller LM, Schwiedrzik JJ, Gasser P, Michler J (2017) Understanding anisotropic mechanical properties ofshales at different length scales: In situ micropillar compression combined with finite element calculations. JGeophys Res: Solid Earth 122(8):5945-5955

Kivi IR, Ameri M, Molladavoodi H (2018) Shale brittleness evaluation based on energy balance analysis of stress-strain curves. J Petrol Sci Eng 167:1–19

Li C, Zhang Z (2019) Modeling shale with consideration of bedding planes by cohesive finite element method. Theor Appl Mech Lett 9(6):397–402

Li Y, Jia D, Rui Z, Peng J, Fu C, Zhang J (2017) Evaluation method of rock brittleness based on statistical constitutive relations for rock damage. J Petrol Sci Eng 153:123–132

Li C, Xie H, Wang J (2020) Anisotropic characteristics of crack initiation and crack damage thresholds for shale. Int J Rock Mech Min Sci 126:104178

Lisjak A, Grasselli G (2014) A review of discrete modeling techniques for fracturing processes in discontinuous rock masses. J Rock Mech Geotech Eng 6(4):301–314

Lisjak A, Liu Q, Zhao Q, Mahabadi OK, Grasselli G (2013) Numerical simulation of acoustic emission in brittle rocks by two-dimensional finite-discrete element analysis. Geophys J Int 195(1):423–443

Lisjak A, Grasselli G, Vietor T (2014) Continuum–discontinuum analysis of failure mechanisms around unsupported circular excavations in anisotropic clay shales. Int J Rock Mech Min Sci 65:96–115

Lisjak A, Young-Schultz T, Li B, He L, Tatone BSA, Mahabadi OK (2020) A novel rockbolt formulation for a GPU-accelerated, finite-discrete element method code and its application to underground excavations. Int J Rock Mech Min Sci 134:104410

Ma T, Peng N, Zhu Z, Zhang Q, Yang C, Zhao J (2018) Brazilian tensile strength of anisotropic rocks: review and new insights. Energies 11(2):304

Ma G, Chen Y, Yao F, Zhou W, Wang Q (2019) Evolution of particle size and shape towards a steady state: insights from FDEM simulations of crushable granular materials. Comput Geotech 112:147–158

Mahabadi OK, Lisjak A, Munjiza A, Grasselli G (2012) Y-Geo: new combined finite-discrete element numerical code for geomechanical applications. Int J Geomech 12(6):676–688

Modiriasari A, Bobet A, Pyrak-Nolte LJ (2017) Active seismic monitoring of crack initiation, propagation, and coalescence in rock. Rock Mech Rock Eng 50(9):2311–2325

Munjiza AA (2004) The combined finite-discrete element method. Wiley, Hoboken

Munoz H, Taheri A, Chanda EK (2016) Rock drilling performance evaluation by an energy dissipation based rock brittleness index. Rock Mech Rock Eng 49(8):3343–3355

Niandou H, Shao JF, Henry JP, Fourmaintraux D (1997) Laboratory investigation of the mechanical behaviour of Tournemire shale. Int J Rock Mech Min Sci 34(1):3–16

Nygård R, Gutierrez M, Bratli RK, Høeg K (2006) Brittle–ductile transition, shear failure and leakage in shales and mudrocks. Mar Pet Geol 23(2):201–212

Ortega JA, Ulm FJ, Abousleiman Y (2007) The effect of the nanogranular nature of shale on their poroelastic behavior. Acta Geotech 2:155–182

Palchik V (2010) Mechanical behavior of carbonate rocks at crack damage stress equal to uniaxial compressive strength. Rock Mech Rock Eng 43(4):497–503

Palchik V, Hatzor YH (2002) Crack damage stress as a composite function of porosity and elastic matrix stiffness in dolomites and limestones. Eng Geol 63(3–4):233–245

Patel R, Zhang Y, Lin CW, Guerrero J, Deng Y, Pharr GM, Xie KY (2022) Microstructural and mechanical property characterization of Argillaceous, Kerogen-rich, and Bituminous shale rocks. J Nat Gas Sci Eng 108:104827

Popp T, Salzer K, Minkley W (2008) Influence of bedding planes to EDZ-evolution and the coupled HM properties of Opalinus Clay. Phys Chem Earth Parts a/b/c 33:S374–S387

Potyondy DO, Cundall PA (2004) A bonded-particle model for rock. Int J Rock Mech Min Sci 41(8):1329–1364

Ramamurthy T, Venkatappa Rao G, Singh J (1988) A strength criterion for anisotropic rocks. In: Australia-New Zealand Conference on Geomechanics, 5th, 1988, Sydney (No. 88/11)

Raynaud S, Ngan-Tillard D, Desrues J, Mazerolle F (2008) Brittle-to-ductile transition in Beaucaire marl from triaxial tests under the CT-scanner. Int J Rock Mech Min Sci 45(5):653–671

Rybacki E, Meier T, Dresen G (2016) What controls the mechanical properties of shale rocks?–Part II: Brittleness. J Petrol Sci Eng 144:39–58

Song H, Zhao Y, Danesh NN, Jiang Y, Li Y (2020a) Uniaxial compressive strength estimation based on the primary wave velocity in coal: considering scale effect and anisotropy. Energy Sources, Part A. https://doi.org/10.1080/15567036.2020.1834644

Song H, Zhao Y, Jiang Y, Du W (2020b) Experimental investigation on the tensile strength of coal: consideration of the specimen size and water content. Energies 13(24):6585

Suo Y, Chen Z, Rahman SS, Chen X (2020) Experimental study on mechanical and anisotropic properties of shale and estimation of uniaxial compressive strength. Energy Sources, Part A. https://doi.org/10.1080/15567036.2020.1779873

Taheri A, Zhang Y, Munoz H (2020) Performance of rock crack stress thresholds determination criteria and investigating strength and confining pressure effects. Constr Build Mater 243:118263

Tarasov B, Potvin Y (2013) Universal criteria for rock brittleness estimation under triaxial compression. Int J Rock Mech Min Sci 59:57–69

Wang J, Xie L, Xie H, Ren L, He B, Li C, Yang Z, Gao C (2016a) Effect of layer orientation on acoustic emission characteristics of anisotropic shale in Brazilian tests. J Nat Gas Sci Eng 36:1120–1129

Wang M, Li P, Wu X, Chen H (2016b) A study on the brittleness and progressive failure process of anisotropic shale. Environ Earth Sci 75(10):1–7

Wang P, Cai M, Ren F (2018a) Anisotropy and directionality of tensile behaviours of a jointed rock mass subjected to numerical Brazilian tests. Tunn Undergr Space Technol 73:139–153

Wang YP, Liu X, Liang LX (2018b) Influences of bedding planes on mechanical properties and prediction method of brittleness index in shale. Lithol Reserv 30(4):149–160 (**(in Chinese)**)

Wang M, Li Z, Shao X (2020) Ultrasonic velocity, attenuation, and mechanical behavior of Longmaxi bedded shale under uniaxial compressive tests. Arab J Geosci 13(19):1–10

Wei D, Zhao B, Dias-da-Costa D, Gan Y (2019) An FDEM study of particle breakage under rotational point loading. Eng Fract Mech 212:221–237

Wu Y, Li Y, Luo S, Lu M, Zhou N, Wang D, Zhang G (2020) Multiscale elastic anisotropy of a shale characterized by cross-scale big data nanoindentation. Int J Rock Mech Min Sci 134:104458

Wu C, Gong F, Luo Y (2021) A new quantitative method to identify the crack damage stress of rock using AE detection parameters. Bull Eng Geol Env 80(1):519–531

Xian H, Zhu J, Tan W, Tang H, Liu P, Zhu R, Liang X, Wei J, He H, Teng HH (2019) The mechanism of defect induced hydroxylation on pyrite surfaces and implications for hydroxyl radical generation in prebiotic chemistry. Geochim Cosmochim Acta 244:163–172

Xue L, Qin S, Sun Q, Wang Y, Lee LM, Li W (2014) A study on crack damage stress thresholds of different rock types based on uniaxial compression tests. Rock Mech Rock Eng 47(4):1183–1195

Yan C, Zheng H, Sun G, Ge X (2016) Combined finite-discrete element method for simulation of hydraulic fracturing. Rock Mech Rock Eng 49(4):1389–1410

Yang SQ, Yin PF, Ranjith PG (2020) Experimental study on mechanical behavior and brittleness characteristics of longmaxi formation shale in Changning, Sichuan basin, China. Rock Mech Rock Eng 53:2461–2483

Yimsiri S, Soga K (2010) DEM analysis of soil fabric effects on behaviour of sand. Géotechnique 60(6):483–495

Yuan H, Li X (2014) Effects of the cohesive law on ductile crack propagation simulation by using cohesive zone models. Eng Fract Mech 126:1–11

Zhai H, Chang X, Wang Y, Lei X, Xue Z (2020) Analysis of acoustic emission events induced during stress unloading of a hydraulic fractured Longmaxi shale sample. J Petrol Sci Eng 189:106990

Zhao XG, Cai M, Wang J, Ma LK (2013) Damage stress and acoustic emission characteristics of the Beishan granite. Int J Rock Mech Min Sci 64:258–269

Zhou W, Yuan W, Ma G, Chang XL (2016) Combined finite-discrete element method modeling of rockslides. Eng Comput 33(5):1530–1559

Zienkiewicz OC, Best B, Dullage C, Stagg KG (1970) Analysis of nonlinear problems in rock mechanics with particular reference to jointed rock systems (No. 364). In: 2nd ISRM Congress